Draft version November 7, 2016
Preprint typeset using LaTeX style AASTeX6 v. 1.0

arXiv:1611.01207v1 [astro-ph.SR] 3 Nov 2016

ON VARIATIONS OF PRE-SUPERNOVA MODEL PROPERTIES

R. Farmer,[1] C.E. Fields,[1,2,3] I. Petermann,[1,3] Luc Dessart,[4] M. Cantiello,[5] B. Paxton,[5] F.X. Timmes[1,3]

[1]School of Earth and Space Exploration, Arizona State University, Tempe, AZ, USA
[2]Department of Physics and Astronomy, Michigan State University, East Lansing, MI 48824, USA
[3]Joint Institute for Nuclear Astrophysics, USA
[4]Universite Côte d'Azur, OCA, CNRS, Lagrange, France
[5]Kavli Institute for Theoretical Physics, University of California, Santa Barbara, CA 93106, USA

ABSTRACT

We explore the variation in single star 15–30 $M_\odot$, non-rotating, solar metallicity, pre-supernova `MESA` models due to changes in the number of isotopes in a fully-coupled nuclear reaction network and adjustments in the mass resolution. Within this two-dimensional plane we quantitatively detail the range of core masses at various stages of evolution, mass locations of the main nuclear burning shells, electron fraction profiles, mass fraction profiles, burning lifetimes, stellar lifetimes, and compactness parameter at core-collapse for models with and without mass loss. Up to carbon burning we generally find mass resolution has a larger impact on the variations than the number of isotopes, while the number of isotopes plays a more significant role in determining the span of the variations for neon, oxygen and silicon burning. Choice of mass resolution dominates the variations in the structure of the intermediate convection zone and secondary convection zone during core and shell hydrogen burning respectively, where we find a minimum mass resolution of $\approx 0.01\, M_\odot$ is necessary to achieve convergence in the helium core mass at the ≈5% level. On the other hand, at the onset of core-collapse we find ≈30% variations in the central electron fraction and mass locations of the main nuclear burning shells, a minimum of ≈127 isotopes is needed to attain convergence of these values at the ≈10% level.

Keywords: stars: evolution — stars: interiors — stars: abundances — supernovae: general

1. INTRODUCTION

The end evolutionary phases of massive stars remain a rich site of fascinating challenges that include the interplay between convection (Meakin & Arnett 2007b; Viallet et al. 2013), nuclear burning (Couch et al. 2015), rotation (Heger et al. 2000; Rogers 2015; Chatzopoulos et al. 2016), radiation transport (Jiang et al. 2015), instabilities (Garaud et al. 2015; Wheeler et al. 2015), mixing (Maeder & Meynet 2012), waves (Rogers et al. 2013; Fuller et al. 2015; Aerts & Rogers 2015), eruptions (Humphreys & Davidson 1994; Kashi et al. 2016), and binary partners (Justham et al. 2014; Marchant et al. 2016). This bonanza of physical puzzles is closely linked with compact object formation by core-collapse supernovae (SN) (Timmes et al. 1996; Eldridge & Tout 2004; Özel et al. 2010) and the diversity of observed massive star transients (e.g., Van Dyk et al. 2000; Ofek et al. 2014; Smith et al. 2016). Recent observational clues that challenge conventional wisdom (Zavagno et al. 2010; Vreeswijk et al. 2014; Boggs et al. 2015; Jerkstrand et al. 2015; Strotjohann et al. 2015), coupled with the expectation of large quantities of data from upcoming surveys (e.g., Creevey et al. 2015; Papadopoulos et al. 2015; Sacco et al. 2015; Yuan et al. 2015), new measurements of key nuclear reaction rates and techniques for assessing reaction rate uncertainties (Iliadis et al. 2011; Wiescher et al. 2012; Sallaska et al. 2013), and advances in 3D pre-SN modeling (Couch et al. 2015; Müller et al. 2016; Jones et al. 2016), offer significant improvements in our quantitative understanding of the end states of massive stars.

One end state, core-collapse SN, is the result of another end state, massive star progenitors undergoing gravitational collapse (e.g., Sukhbold & Woosley 2014; Perego et al. 2015; Sukhbold et al. 2016). The amount of mass of an isotope that can be injected into the interstellar medium (e.g., Woosley & Weaver 1995; Limongi & Chieffi 2003; Nomoto et al. 2013) depends on the structure of the star at the point of core-collapse. In turn, the pre-SN structure depends on the evolutionary pathway taken by the massive star during its lifetime (e.g., Nomoto & Hashimoto 1988; Jones et al. 2013).

rjfarmer@asu.edu

This paper is novel in two ways. First, we scrutinize the structure and evolution of single massive stars from the pre-main sequence (pre-MS) to the onset of core-collapse with multiple, possibly large, in-situ nuclear reaction networks. For the first time, we quantify aspects of the structure and evolution that are robust, or can be made robust, with respect to variations in the nuclear reaction network used for the entire evolution. For example, we explore the diversity of pre-SN model properties such as the mass locations of the major burning stages, core masses at various stages of evolution, mass fraction profiles, and electron fraction profiles. Second, for each nuclear reaction network we investigate the impact of methodically and systematically changing the mass resolution on the structure and evolution of a set of massive stars.

In §2 we discuss the software instruments, input physics, reaction networks, and model choices. In §3 we present the results for different reaction networks, and mass resolutions with and without mass loss. In §4 we discuss our results and their implications.

2. STELLAR MODELS

Models of 15, 20, 25 and 30 $M_\odot$ are evolved using the Modules for Experiments in Stellar Astrophysics software instrument (henceforth `MESA`, version 7624, Paxton et al. 2011, 2013, 2015). All models begin with a metallicity of $Z = 0.02$ and a solar abundance distribution from Grevesse & Sauval (1998). The models are evolved without mass loss or with the "Dutch" wind loss scheme (Nieuwenhuijzen & de Jager 1990; Nugis & Lamers 2000; Vink et al. 2001; Glebbeek et al. 2009) with an efficiency η=0.8 for these non-rotating models (Maeder & Meynet 2001). Each stellar model is evolved from the pre-MS until core-collapse, which we take as when any location inside the stellar model reaches an infall velocity of 1000 km s^{-1}. To compute the infall velocity we set `MESA`'s `v_flag=.true.` which adds a, hydrodynamic, radial velocity term to the model. This additional variable is evolved from the zero-age main sequence (ZAMS) until core-collapse, though it only becomes relevant to the evolution after core oxygen burning.

All the `MESA` inlists and many of the stellar models are publicly available[1].

2.1. *Mass and Temporal Resolution*

`MESA` provides several controls to specify the mass resolution of a model. Sufficient mass resolution is required to accurately determine gradients of stellar structure quantities, but an excessive number of cells impacts performance. One parameter for changing the mass resolution in regions of rapid change is `mesh_delta_coeff` ($\delta_{\rm mesh}$), which acts a global scale factor limiting the change in stellar structure quantities between two adjacent cells. Smaller values of $\delta_{\rm mesh}$ increases the number of cells. Another parameter controlling mass resolution is the maximum fraction a star's mass in a cell, `max_dq`. That is, the minimum number of cells in a stellar model is $1/$`max_dq`. We use $\delta_{\rm mesh} = 1.0$ and `max_dq` $= \Delta M_{\rm max}/M_\star(\tau)$, where $M_\star(\tau)$ is the mass of the stellar model in solar mass units at time τ and $\Delta M_{\rm max}$ is a parameter we vary between $0.1\,M_\odot$ and $0.005\,M_\odot$. We choose to vary `max_dq` instead of `mesh_delta_coeff` to enable us to set a minimum level of mass resolution in the model.

`MESA` also offers a rich set of timestep controls. The parameter w_t broadly controls the temporal resolution by modulating the magnitude of the allowed changes between time steps. At a finer level of granularity, `dX_nuc_drop_limit` limits the maximum allowed change of the mass fractions between timesteps for mass fractions larger than `dX_nuc_drop_min_X_limit`. We use $w_t = 5 \times 10^{-5}$, `dX_nuc_drop_limit` $= 10^{-3}$, and `dX_nuc_drop_min_X_limit` $= 10^{-3}$ for evolution between the pre-MS to the onset of core Si-burning, where we loosen the criteria to allow larger timesteps; $w_t = 5 \times 10^{-5}$, `dX_nuc_drop_limit` $= 5 \times 10^{-2}$, and `dX_nuc_drop_min_X_limit` $= 5 \times 10^{-2}$.

The timestep control `delta_lg_XH_cntr_min` regulates the timestep as hydrogen is depleted in the core, which aids resolving the transition from the ZAMS to the terminal age main sequence (TAMS). Similarly, the timestep controls `delta_lg_XHe_cntr_min`, `delta_lg_XC_cntr_min`, `delta_lg_XNe_cntr_min`, `delta_lg_XO_cntr_min`, and `delta_lg_XSi_cntr_min` control the timestep as one of the major fuels is depleted in the core. These timestep controls are useful for obtaining, for example, convergence of mass shell locations, smoother transitions as a stellar model exits core H-burning in the HR diagram (i.e., the "Henyey Hook", Kippenhahn et al. 2012), and smoother trajectories in the central temperature $T_{\rm c}$ - central density $\rho_{\rm c}$ plane. We use a mass fraction value of 10^{-6} for all these fuel depletion timestep controls. Additionally, we use `MESA`'s default timestep controls for controlling changes in the hydrodynamics. At the point where hydrodynamics becomes important, during Si burning, we find we are limited by the `delta_lg_XSi_cntr_min` control rather than by changes in the hydrodynamics.

2.2. *Nuclear Reaction Networks*

`MESA` evolves models of massive stars from the pre-MS to the onset of core-collapse with the nuclear burning fully coupled to the hydrodynamics using a single, possibly large, reaction network (see Paxton et al. (2015)).

[1] http://mesastar.org/results

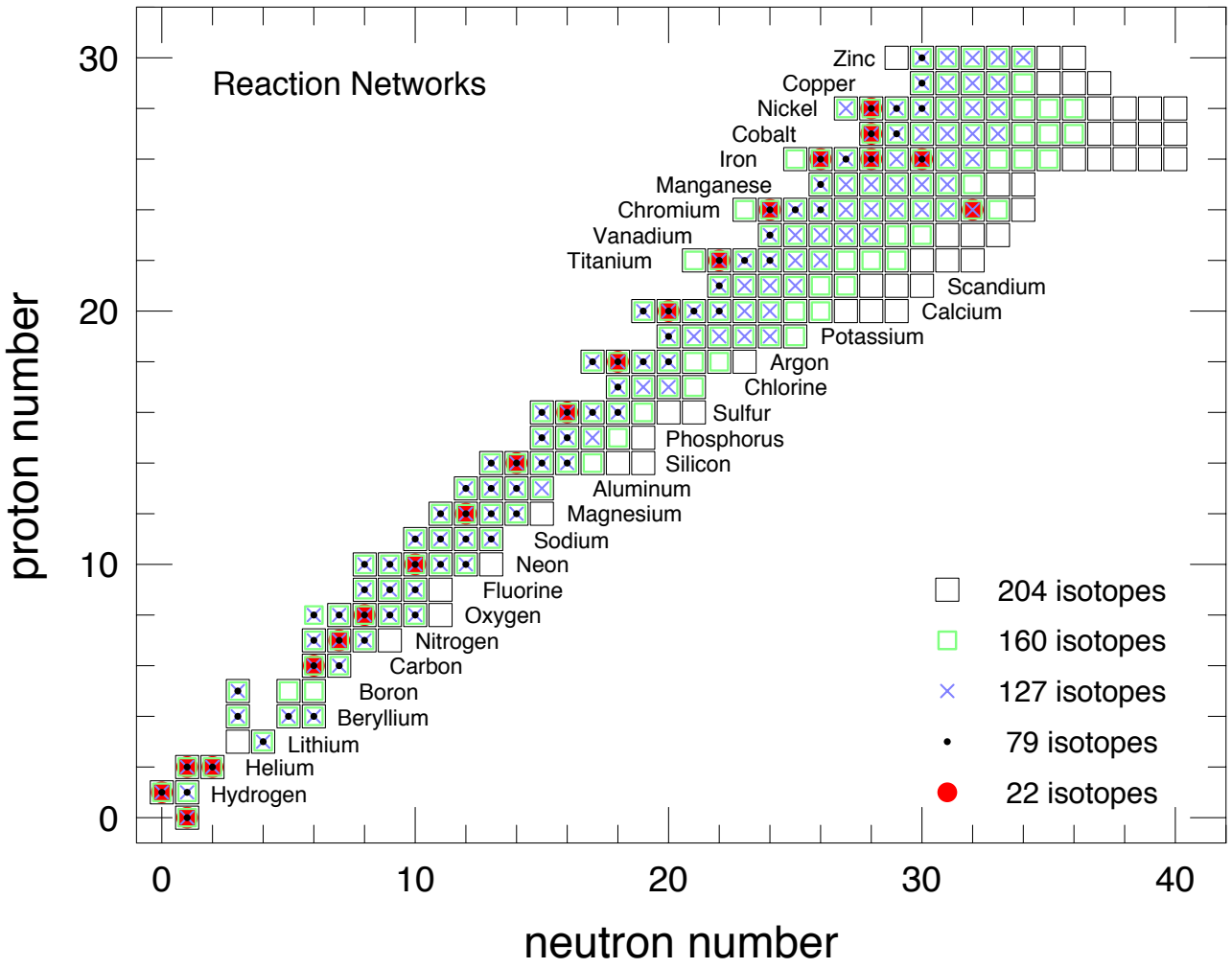

Figure 1. The five reaction networks used to quantify the variance of the properties of the pre-SN cores as a function of the number of isotopes in a network.

This capability avoids the challenges of a) operator splitting errors from evolving the hydrodynamics and nuclear burning independently; b) stitching together different solution methods for different phases of evolution, for example, combining a reaction network with equilibrium methodologies like QSE or NSE, or with the use of an adaptive network that modifies itself based on the most populous isotopes present; or finally c) evolving a stellar model with a small reaction network while carrying along a larger reaction network that does not impact the energy generation rate or composition of the stellar structure, i.e., passive co-processing. `MESA`'s unified approach is not just a solution to issues of accuracy or self-consistency. It offers an improvement by providing a single solution methodology – in situ reaction networks evolved simultaneously with the hydrodynamics.

We evolve each stellar model with one of the five nuclear reaction networks shown in Figure 1. We consider a small network, `approx21_cr60_plus_co56.net` (hereafter `approx22.net`), where each reaction pathway has been predetermined (i.e., a "hardwired" network). Such approximate networks, an α-chain backbone with aspects of H-burning, heavy ion reactions, and iron-group photodisintegration, are a traditional workhorse in massive star models (e.g., Weaver et al. 1978; Woosley & Weaver 1988; Heger et al. 2000; Heger & Woosley 2010; Chatzopoulos & Wheeler 2012). We also use four "softwired" networks, where after specifying the isotopes, all allowed reaction pathways between the isotopes are linked. Specifically, we consider `mesa_79.net` which contains isotopes up to ^{60}Zn (black dots); `mesa_127.net` which adds neutron rich isotopes in the iron group (purple crosses); `mesa_160.net` which adds more neutron rich isotopes and a few proton rich isotopes (green squares); and `mesa_204.net` which adds isotopes lighter than ^{36}Cl (black squares), and includes the isotopes identified in Heger et al. (2001) as important for the electron fraction, Y_e, in core-collapse models.

The softwired reaction networks are designed to yield approximately the same final Y_e as a 3298 isotope re-

action network in one-zone burn calculations of the thermodynamic history of $15\,M_\odot$ cores (Paxton et al. 2015). For example, in one-zone burn calculations the `mesa_204.net` reaction network gives a final $Y_e = 0.4032$, while the 3298 isotope reaction network gives $Y_e = 0.4039$.

All forward thermonuclear reaction rates are from the JINA reaclib version V2.0 2013-04-02 (Cyburt et al. 2010). Inverse rates are calculated directly from the forward rates (those with positive Q-value) using detailed balance, rather than using fitted rates. The nuclear partition functions used to calculate the inverse rates are from Rauscher & Thielemann (2000). Electron screening factors for both weak and strong thermonuclear reactions are from Alastuey & Jancovici (1978) with plasma parameters from Itoh et al. (1979). All the weak rates are based (in order of precedence) on the tabulations of Langanke & Martínez-Pinedo (2000), Oda et al. (1994), and Fuller et al. (1985). Thermal neutrino energy losses are from Itoh et al. (1996).

2.3. *Mixing*

We treat convection using the `mlt++` approximation (Paxton et al. 2013). This prescription takes the convective strength as computed by mixing length theory (MLT) and reduces the superadiabaticity in radiation dominated convection zones (e.g., near the iron opacity peak). This decreases the temperature gradient in these regions and the artificial suppression can be viewed as treating additional, un-modeled, energy transport mechanisms in these regions (e.g., Jiang et al. 2015). Values of $1.6 \lesssim \alpha_{\rm MLT} \lesssim 2.2$ have been inferred from comparing observations with stellar evolution models (Noels et al. 1991; Miglio & Montalbán 2005; Aerts et al. 2010), and 3D hydrodynamic simulations of the deep core and surface layers also suggests a similar range (Viallet et al. 2013; Trampedach et al. 2014; Jiang et al. 2015). These efforts inform our baseline choice of $\alpha_{\rm MLT}$=1.5, though this is by no means the only choice (Dessart et al. 2013).

Convective overshooting is assumed to be an exponential decay beyond the Schwarzschild boundary of convection (Herwig et al. 1997). The convective diffusion coefficient, $D_{\rm conv,0}$, is measured at a distance $f_{\rm ov,D}$ inside the convection zone, overshooting then extends beyond the edge of the convection zone a fraction $f_{\rm ov}$ of the local pressure scale height $\lambda_{\rm P,0}$,

$$D_{\rm OV} = D_{\rm conv,0} \exp\left(-\frac{2z}{f_{\rm ov}\lambda_{\rm P,0}}\right) \ , \qquad (1)$$

where $D_{\rm OV}$ is the overshooting diffusion coefficient at a radial distance z from the edge of the convection zone boundary. Our baseline choices for the overshoot mixing are $f_{\rm ov} = 0.004$ and $f_{\rm ov,D} = 0.001$. This choice is motivated by recent calibration of a 1D $25\,M_\odot$ pre-SN model to idealized 3D hydrodynamic simulations of turbulent O-burning shell convection (Jones et al. 2016). `MESA` offers the flexibility to have different values for convection driven by different types of nuclear burning (H, He, C and others) and whether the burning occurs near the core or in a shell, but for simplicity we take these values to be the same for all regions.

Thermohaline mixing is included in the models when $\nabla_{\rm T} - \nabla_{\rm ad} \leq B \leq 0$, where B is the Brünt composition gradient. The thermohaline mixing diffusion coefficient $D_{\rm th}$ is parameterized as

$$D_{\rm th} = \alpha_{\rm th} \frac{3K}{2\rho C_p} \frac{B}{(\nabla_{\rm T} - \nabla_{\rm ad})} \ , \qquad (2)$$

where $\alpha_{\rm th}$ is a dimensionless parameter, K is the radiative conductivity, and $C_{\rm p}$ is the specific heat at constant pressure (Ulrich 1972; Kippenhahn et al. 1980). Continuing attempts to calibrate $D_{\rm th}$ include multidimensional simulations of fingering convection under stellar conditions (Traxler et al. 2011; Brown et al. 2013; Garaud et al. 2015). We set $\alpha_{\rm th}$=2.0 except during core silicon burning where we set $\alpha_{\rm th}$=0.0.

Finally, we include semiconvection when $\nabla_{\rm ad} < \nabla_{\rm T} < \nabla_{\rm L}$, where $\nabla_{\rm L} = \nabla_{\rm ad} + B$. We take the strength of semiconvective mixing $D_{\rm semi}$ as Langer et al. (1983, 1985),

$$D_{\rm sc} = \alpha_{\rm sc} \left(\frac{K}{6C_p\rho}\right) \frac{\nabla_{\rm T} - \nabla_{\rm ad}}{\nabla_{\rm L} - \nabla_{\rm T}}, \qquad (3)$$

where $\alpha_{\rm sc}$ is a dimensionless parameter. Ongoing efforts to calibrate 1D semiconvection models include multidimensional simulations of double diffusive convection (Zaussinger & Spruit 2013; Spruit 2013) and comparing massive star models with observations (Yoon et al. 2006). While recent work suggests that to a first order approximation, the effect of semiconvection can be neglected (Moll et al. 2016), we adopt a baseline choice of $\alpha_{\rm sc} = 0.01$.

3. RESULTS

We present the variations in the `MESA` version 7624 pre-SN model properties due to changes in the nuclear reaction network and mass resolution in the order of the major burning stages; H-burning in §3.1, stellar lifetimes in §3.2, He-burning in §3.3, C-burning in §3.4, Ne-burning in §3.5, O-burning in §3.6, Si-burning in §3.7, the onset of core-collapse in §3.8, and representative pre-SN nucleosynthesis yields in §3.9.

3.1. *Core/Shell H burning*

Figure 2 shows the MS and giant branch (GB) evolution of a $15\,M_\odot$ model at two resolutions $\Delta M_{\rm max} = 0.1\,M_\odot$ and $\Delta M_{\rm max} = 0.005\,M_\odot$, evolved without mass loss and with the `approx22.net` network. As stars evolve off of the pre-MS and onto the ZAMS, they begin

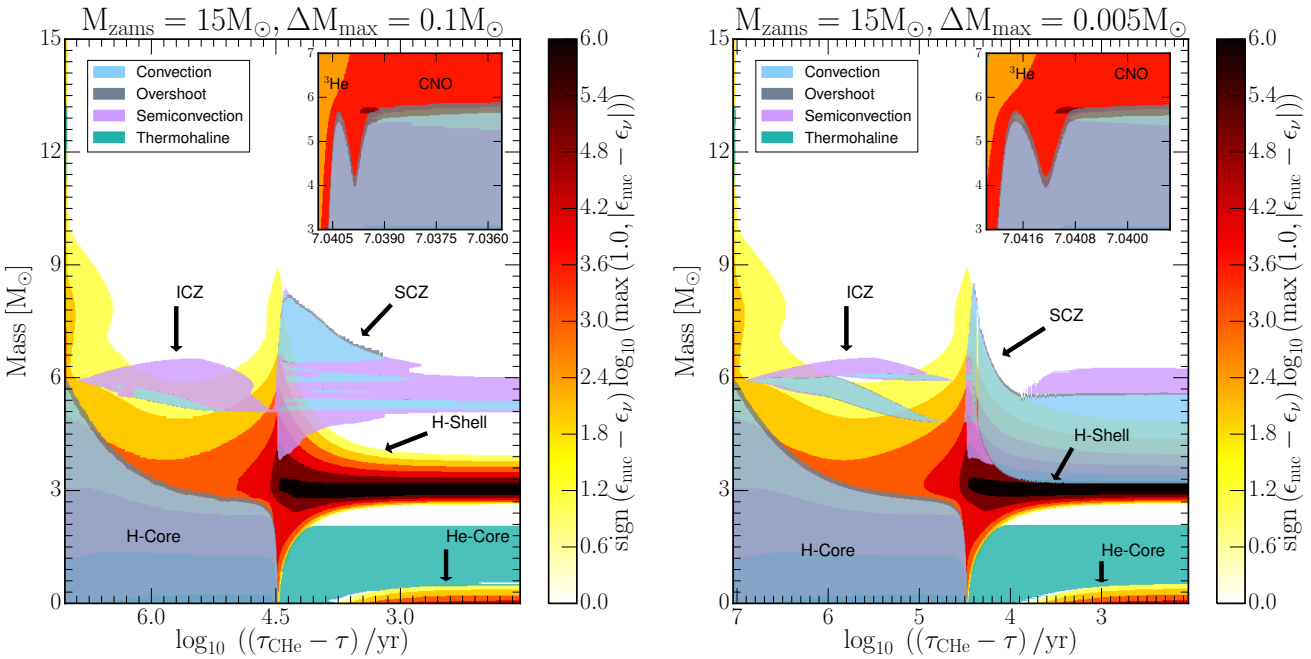

Figure 2. Kippenhahn plot for a solar metallicity $M_{ZAMS} = 15\,M_\odot$ model evolved with the `approx22.net` and without mass loss. Left panel, mass resolution of $\Delta M_{max} = 0.1\,M_\odot$; Right panel, mass resolution of $\Delta M_{max} = 0.005\,M_\odot$. The age shown on the x-axis is time until convection begins in core He-burning, set such that the SCZ can be temporally resolved. Yellow to red regions denote logarithmic increases in the net nuclear energy generation rate. Blue marks convective regions, grey identifies overshoot regions, purple designates semiconvective regions and green labels thermohaline mixing regions. Labeled are the intermediate convection zone (ICZ), secondary convection zone (SCZ), H-core, H-shell, and He-core. The inset Kippenhahn diagram shows the behavior of the convective core during the transition between ^{3}He and CNO burning.

burning hydrogen in a convective core, predominantly via the CNO cycle, but also via primordial ^{3}He in the *pp* chain (Hansen et al. 2004; Iben 2013a,b). This convective region expands outwards to consume approximately half the mass of the star. Once the primordial ^{3}He is exhausted, at $\log_{10}((\tau_{CHe} - \tau)/yr) \approx 7.04$ in Figure 2, the convection region recedes and the core temperature and density increase. At this point in the evolution most of the primordial ^{12}C is already piled up in ^{14}N due to the proton capture onto ^{14}N reaction rate (Arnett 1996; Iliadis 2007). Due to the strong temperature dependence of the CNO cycle, the energy production increases and the convective region expands slightly further out in mass coordinate than the first peak at $\log_{10}((\tau_{CHe} - \tau)/yr) \approx 7.039$. Due to the increased energy generation from the CNO cycle the star itself also begins expanding at this point.

The convective core shrinks during core H-burning. This recession leaves behind a composition gradient (μ−gradient, ∇_μ) and lower levels of nuclear burning. Our models form a layered structure of semiconvective and convective regions, labeled an intermediate convection zone (ICZ) in Figure 2, at $\log_{10}((\tau_{CHe} - \tau)/yr) \approx 5.75$ at the approximate mass coordinate of the maximal extent of the core convection zone ($\approx 6\,M_\odot$) (Langer et al. 1985; Heger et al. 2000; Hirschi et al. 2004). As the mass resolution or the initial mass of the stellar model increases the structure and behavior the ICZ changes. For the $M_{ZAMS} = 15\,M_\odot$ models, in Figure 2, when the mass resolution is increased from $\Delta M_{max} = 0.1\,M_\odot$ to $\Delta M_{max} = 0.005\,M_\odot$, the fraction (in mass coordinates) of semiconvection in the ICZ decreases while the amount of convection increases.

Figure 2 shows that as the mass resolution increases the fine structure of the H-core convection zone, the maximal extent of the H-core extent and the edge of the overshoot region are better determined. All of which determine how much fresh H fuel is pulled into the core during the MS and how much fuel is available just outside the convective core to form the ICZ. At higher resolution less hydrogen is burned when the ICZ forms, which makes the star more compact due to the decreased burning. As less hydrogen has been burned, ∇_μ is smaller.

Semiconvection occurs when $\nabla_{ad} < \nabla_T < \nabla_L$ where ∇_L is a function of ∇_μ. If ∇_μ is large enough it can maintain a semiconvective region over the entire ICZ. If ∇_μ is small in a local region, then the semiconvective region may transition into a convective region (Langer et al. 1985). This occurs in Figure 2 in the higher resolution $\Delta M_{max} = 0.005\,M_\odot$ panel where ∇_μ is smaller, allowing more convection to develop inside the semicon-

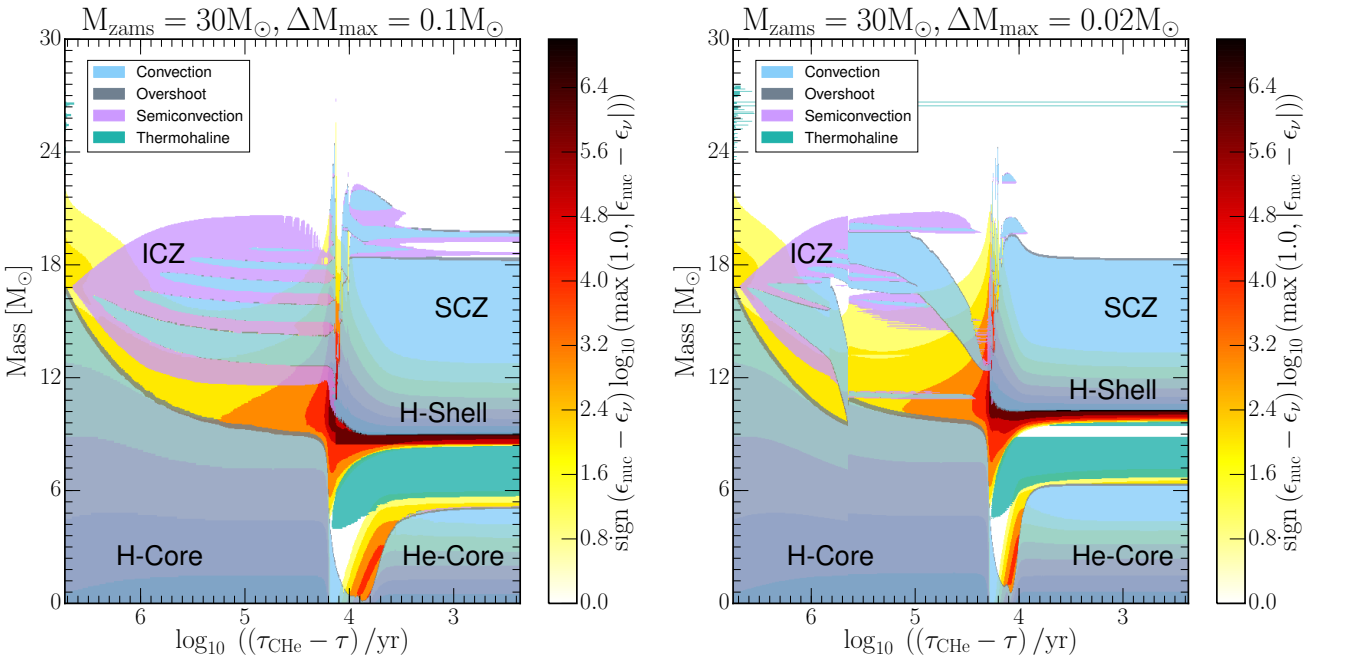

Figure 3. Same as Figure 2 but for a solar metallicity $M_{\rm ZAMS} = 30\,{\rm M}_\odot$ model evolved with the `mesa_79.net` and without mass loss. The left panel is for a mass resolution of $\Delta{\rm M}_{\rm max} = 0.1\,{\rm M}_\odot$, and the right panel is for a mass resolution of $\Delta{\rm M}_{\rm max} = 0.02\,{\rm M}_\odot$. As convection never ceases in the core, the x-axis is set such that it has a similar scale as Figure 2, and is measured until an arbitrary point during core helium burning.

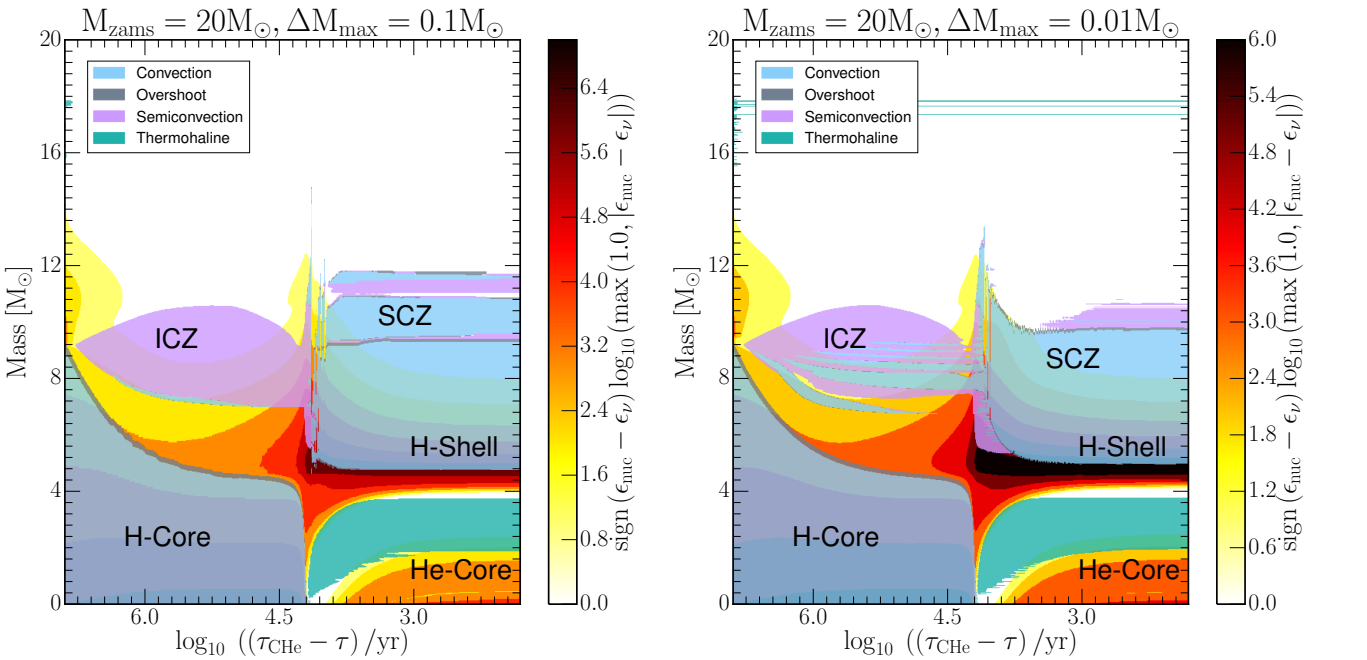

Figure 4. Same as Figure 2 but for a solar metallicity $M_{\rm ZAMS} = 20\,{\rm M}_\odot$ model evolved with the `mesa_127.net` and mass loss. The left panel corresponds to mass resolution of $\Delta{\rm M}_{\rm max} = 0.1\,{\rm M}_\odot$, while the Right panel corresponds to a mass resolution of $\Delta{\rm M}_{\rm max} = 0.01\,{\rm M}_\odot$. The age shown on the x-axis is the time until convection begins in the He core. Note the change in color bar scale between the left and right panels; lower mass resolution models release more energy during H-shell burning.

vective region (Mowlavi & Forestini 1994). This is most clearly seen as the bifurcation of the ICZ in the lower resolution $\Delta{\rm M}_{\rm max} = 0.1\,{\rm M}_\odot$ (left panel), while in the right panel the convection zone is embedded inside the semiconvective region. Higher mass resolutions also capture the substructure in the $\nabla_{\rm L}$, which become the seeds for the convective regions to form.

Langer et al. (1985) showed similar variations in the

ICZ structure by varying the strength of the α_{sc} parameter. As the efficiency of semiconvection increases, the fine structure increases. Our MESA models achieve a similar result by varying the mass resolution for a fixed α_{sc}.

A secondary convective zone (SCZ) then forms, at $\log_{10}((\tau_{CHe} - \tau)/\mathrm{yr}) \approx 4.5$, when H-shell burning begins, in both models. Figure 2 shows how the structure and behavior of the SCZ changes with mass resolution. The low resolution model (left panel) has layered semiconvection/convection that stays outside of the H-shell. In the higher resolution model (right panel), the SCZ is dominated by convection which propagates into the H-shell burning region. This merger of the SCZ and the H-shell leads to fresh fuel being injected into the H-shell and allows the star to live longer. If the star has mass loss, then the longer H-burning lifetimes create larger He-cores which will last longer and thus increase the amount of mass lost (§3.2).

This difference in behavior is due to the SCZ forming within the mass coordinates previously occupied by the ICZ semiconvective/convective mixing region. The larger convectively mixed region during the ICZ in the higher resolution model implies that the $\mu-$gradient left behind by the receding H-core is reduced or even zero. In turn, this reduction in the $\mu-$gradient allows convection to form over a larger mass range in the SCZ. That is, a preceding semiconvective phase is not necessary to reduce the $\mu-$gradient. This is shown in Figure 2 by the relative difference in mass covered by semiconvection and convection at $\log_{10}((\tau_{CHe} - \tau)/\mathrm{yr}) \approx 4.5$.

The $M_{ZAMS} = 30\,M_\odot$ models without mass loss are qualitatively similar, and Figure 3 shows a representative set of MESA models. When the ICZ forms, multiple layers of alternating semiconvection and convection form (Langer et al. 1985). At lower mass resolutions (left panel) this structure begins at $M \approx 17\,M_\odot$ and propagates inward to $M \approx 13\,M_\odot$. As the mass resolution increases (right panel), the convective fingers start at a similar mass coordinate but will propagate deeper into the star. Figure 3 shows an example of the fingers moving sufficiently inwards to penetrate the H-burning core. There is a brief increase in the nuclear burning, as shown by the near step function in burning at $\log_{10}((\tau_{CHe} - \tau)/\mathrm{yr}) \approx 5.5$ due to the ICZ injecting unburnt hydrogen into the core. This leads to a longer MS lifetime for these models. This penetration of the core is a binary process, either the ICZ penetrates the core or it does not. Thus, one may expect step functions in the MS lifetime (§3.2).

For the $M_{ZAMS} = 20\,M_\odot$ models with mass loss, Figure 4 shows a third possible state. As the mass resolution increases the SCZ, which formed at the TAMS, decreases in extent. The left panel of Figure 4 shows that for a relatively coarse mass resolution of $\Delta M_{max} = 0.1\,M_\odot$ the SCZ forms multiple convection/semiconvection zones out to $M \approx 12\,M_\odot$, while the right panel shows that for a finer mass resolution of $\Delta M_{max} = 0.01\,M_\odot$ the SCZ forms a single convection zone out to $M \approx 10\,M_\odot$. The increased extent of the SCZ region allows more hydrogen fuel to be mixed inwards towards the core, and increases the hydrogen mass fraction by a few percent at the H-burning shell. This allows the H-shell to burn more energetically and for longer. Thus we would expect the models with lower spatial resolution to evolve slower to core collapse, but this effect is limited due to the small change in hydrogen mass fraction.

3.2. *Stellar Lifetimes*

Figure 5 shows the lifetime for the non mass losing models (top panel) and for models with mass loss (bottom panel). The most striking feature is the sharp bifurcation of the lifetimes as a function of mass resolution, most prominently seen in the $M_{ZAMS} = 15\,M_\odot$ and $30\,M_\odot$ models without mass loss at a spatial resolution of $\Delta M_{max} = 0.05\,M_\odot$. This is a direct consequence of the differences in behavior of the ICZ and SCZ during the MS and GB phases. Models where the ICZ penetrate the MS H-core, or where the SCZ penetrates the H-shell as in the $15\,M_\odot$ models, live up to $\approx 5\%$ longer due to the injection of fresh hydrogen fuel. Models with hatching indicate those that do not reach core-collapse, though all reach at least Si burning. Thus we include them in our comparisons up to Si burning.

Stellar models with and without mass loss have similar ages, with a trend for stars with mass loss to have shorter lifetimes (e.g., El Eid et al. 2004). The spread in age is larger for models without mass loss than those with mass loss. This is chiefly due to differences in the size of the timesteps, thus this is a numerical artifact. While all models have the same temporal control w_t, those with mass loss require a smaller timestep to keep the variation per step within the limits specified by w_t. Smaller timesteps allow the mass lost to be treated more accurately, as the amount of mass loss per step depends on the stellar parameters at the start of the step, thus smaller timesteps will better capture fast changes in the star's structure.

Compared to the pre-SN lifetimes from Paxton et al. (2011), Limongi et al. (2000), Woosley et al. (2002), and Hirschi et al. (2004), we find in general, the total stellar lifetimes considered agree to within $\approx \pm 5\%$. The models of Woosley et al. (2002) tend to predict longer lifetimes. Specifically, for the $M_{ZAMS} = 15\,M_\odot$ model, they predict an $\approx 3\%$ longer lifetime until core-collapse. This value increases to $\approx 7\%$ for the $M_{ZAMS} = 25\,M_\odot$ model. Limongi et al. (2000) predict shorter lifetimes with $\approx 7\%$

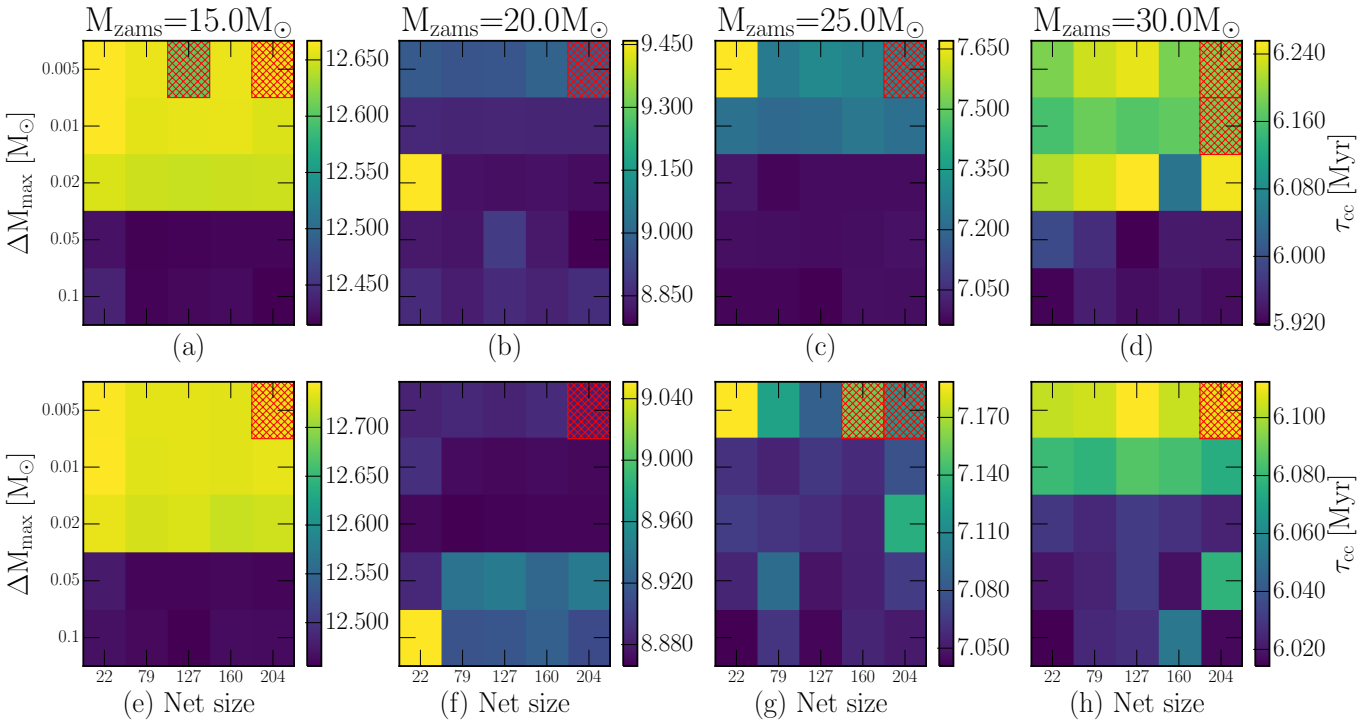

Figure 5. Lifetimes in mega years till core collapse as a function of mass resolution and number of isotopes in the nuclear reaction network. Top panel: models without mass loss, Bottom panel: models with mass loss. Hatching indicate models that did not reach core-collapse, but do reach silicon burning.

difference for their $M_{ZAMS} = 25\,M_\odot$ model. The models of Paxton et al. (2011) and Hirschi et al. (2004) agree with our values to within $\lesssim 1\%$ for $M_{ZAMS} = 15$ and $20\,M_\odot$ models, and spread to $\pm 2\%$ for $M_{ZAMS} = 25\,M_\odot$. Each set of pre-SN models considered here for comparison use a slightly differing set of input physics. For example, our models use a more efficient value for convective overshoot than in the Paxton et al. (2011) models and consider larger nuclear reaction networks. In addition, each set of pre-SN models considered use different (and often unspecified) mass and temporal resolutions. We find considerable agreement among the total stellar lifetimes, with the largest discrepancies occurring at $M_{ZAMS} = 25\,M_\odot$.

Models with the same mass resolution show little variation in the final age with respect to changes in the number of isotopes in the reaction network. For example, the $M_{ZAMS} = 15\,M_\odot$ models with and without mass loss in Figure 5 show uniformity in the stellar age as a function of network size on either side of the bifurcation point. This is due to efficient mixing of the composition by convection; it does not make much difference where or when the SCZ penetrates the H-shell, for once it does, the H-shell is injected with similar amounts of fresh fuel (see Figure 2). As the initial mass of the stellar model increases, the magnitude of the spread in the stellar lifetime decreases. This is due to smaller variations in when and where the ICZ penetrates the H-core.

There are outlier models for the smallest network, `approx22.net`: the $M_{ZAMS} = 20\,M_\odot$ model without mass loss and $\Delta M_{max} = 0.02\,M_\odot$, the $M_{ZAMS} = 25\,M_\odot$ model without mass loss and $\Delta M_{max} = 0.005\,M_\odot$, and the $M_{ZAMS} = 20\,M_\odot$ model with mass loss and $\Delta M_{max} = 0.1\,M_\odot$. These are caused by the SCZ penetrating deep into the star, from the edge of the H-burning shell to the radiative region at the center of the star. This injects enough unburnt hydrogen to prolong the lifetimes.

The $M_{ZAMS} = 20\,M_\odot$ models without mass loss in Figure 5 show a lifetime bifurcation at a finer spatial resolution of $\Delta M_{max} = 0.005\,M_\odot$ than the $M_{ZAMS} = 15\,M_\odot$. In addition, the $M_{ZAMS} = 20\,M_\odot$ models with mass loss show the bifurcation is inverted – increasing resolution decreases the stars lifetime – due to the relative extent of the SCZ region discussed for Figure 4.

For the $M_{ZAMS} = 25\,M_\odot$ and $30\,M_\odot$ models, Figure 5 shows the lifetime bifurcation point varies depending on whether there is mass loss or not. The stars without mass loss bifurcate at $\Delta M_{max} = 0.01\,M_\odot$ and $\Delta M_{max} = 0.02\,M_\odot$ respectively, while the mass losing models bifurcate at $\Delta M_{max} = 0.005\,M_\odot$ and $\Delta M_{max} = 0.01\,M_\odot$, effectively one level of resolution higher. This variation may be due to our grid of mass resolutions being insufficient to resolve the bifurcation.

We encourage careful consideration of the mass resolution when modeling massive stars with `MESA`. Not

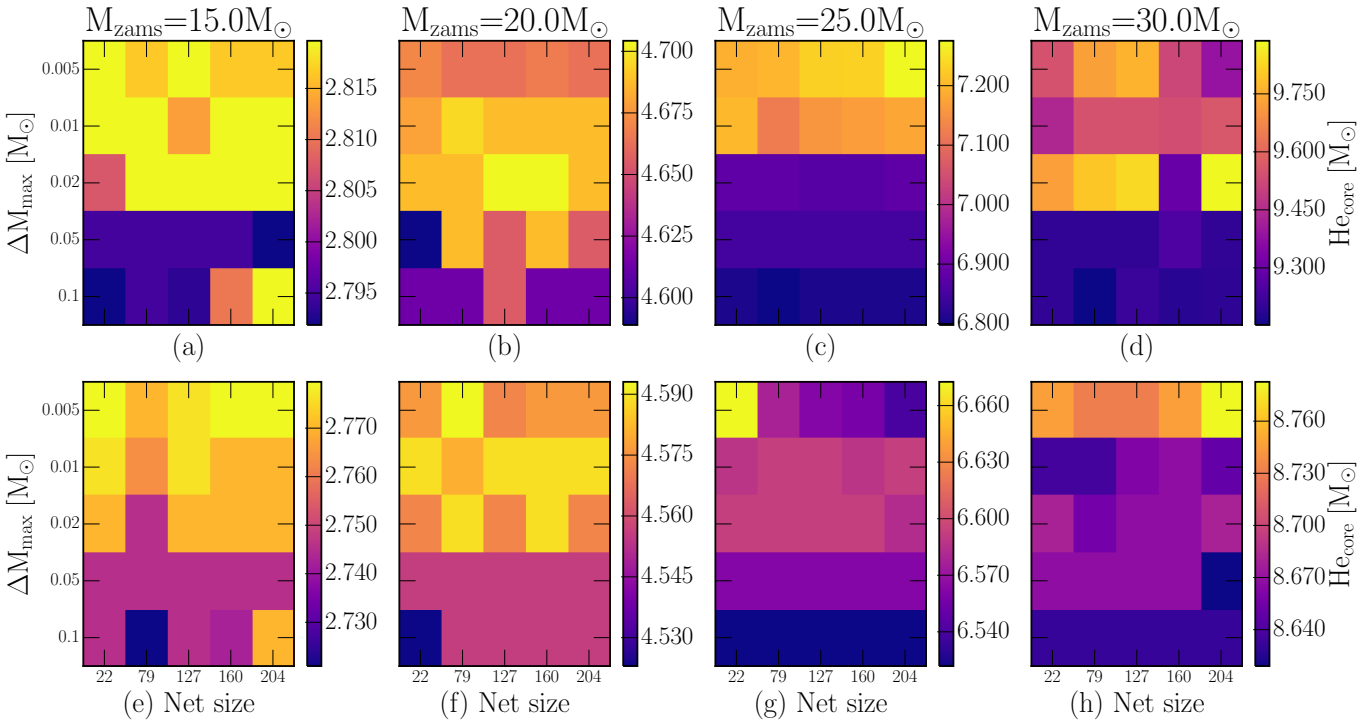

Figure 6. The ^{4}He core mass at the formation of the He core, defined as where $X(^1\mathrm{H}) < 0.01$ and $X(^4\mathrm{He}) > 0.1$. Top panel: `MESA` models without mass loss, Bottom panel: models with mass loss.

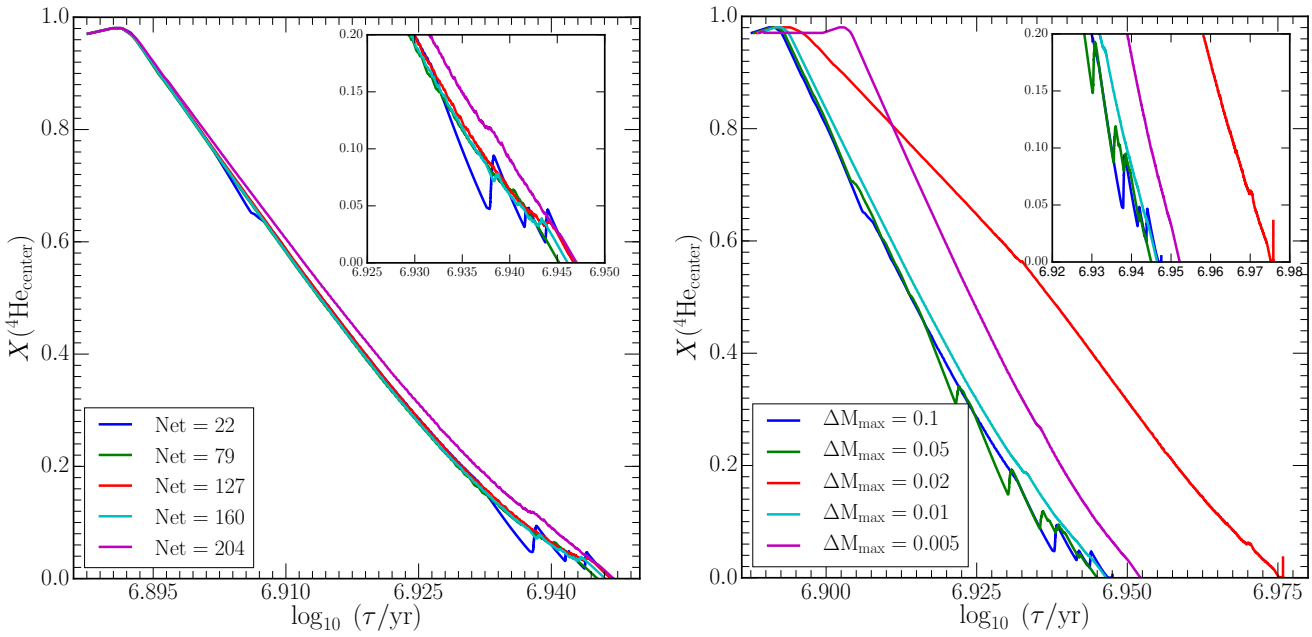

Figure 7. Mass fraction of ^{4}He as a function of time during core He-burning for the $\mathrm{M_{ZAMS}} = 20\,\mathrm{M_\odot}$ models without mass loss. Left panel: models as a function of number of isotopes for a fixed resolution of $\Delta\mathrm{M_{max}} = 0.1\,\mathrm{M_\odot}$. Right panel: models as a function of mass resolution for a fixed `approx22.net` network. The inserts show a zoom in when $X(^4\mathrm{He}) < 0.2$.

only to the choice `MESA`'s δ_{mesh} parameter, which only increases the number of zones if `MESA` detects a large enough spatial gradient, but also the number of zones used throughout the model. Much of the variation seen in the MS and GB phases is set by the stellar structure at the start of the MS, which is early enough that δ_{mesh} may not have sufficient time to act. From Figures 5 and for our choice of α_{sc}, we recommend a mass resolution of at least $\Delta\mathrm{M_{max}} = 0.01\,\mathrm{M_\odot}$, which equates to at least ≈ 2000 mass cells during the pre-MS and MS evolution

in order to reasonably resolve the ICZ and SCZ features. In addition, we recommend temporal controls that limit the timestep as major fuels are depleted in the core (see §2.1).

3.3. *Core He-burning*

Figure 6 shows the He-core mass at the onset of convective core He-burning as a function of mass resolution ΔM_{max} and the number of isotopes in the nuclear reaction network. We define the He-core mass as the location where $X(^4He) > 0.1$ and $X(^1H) < 0.01$ and measured when the star reaches the base of the GB. They share many of the same features – bifurcations and outliers – discussed for the stellar lifetimes in Figure 5. For the $M_{ZAMS} = 15\,M_\odot$ models without mass loss the initial He-core mass ranges from ≈ 2.79 to $2.81\,M_\odot$, while models with mass loss span ≈ 2.72 to $2.77\,M_\odot$. For the $M_{ZAMS} = 20\,M_\odot$ models without mass loss the initial He-core mass range between ≈ 4.6 to $4.7\,M_\odot$, while models with mass loss span between ≈ 4.5 to $4.6\,M_\odot$. Our $M_{ZAMS} = 25\,M_\odot$ models without mass loss show initial He-core mass ranges of ≈ 6.8 to $7.2\,M_\odot$, while models with mass loss span ≈ 6.54 to $6.66\,M_\odot$. The $M_{ZAMS} = 30\,M_\odot$ models without mass loss show the initial He-core mass ranges between ≈ 9.2 to $9.8\,M_\odot$, while models with mass loss spans ≈ 8.63 to $8.78\,M_\odot$. In general, a longer core H-burning phase produces a larger He-core mass. The initial He-core masses in Figure 6 and their range as a function of mass resolution and number of isotopes in the reaction network are commensurate with the He-core masses found in numerous studies (e.g., Nomoto & Hashimoto 1988; Langer 1991; Wellstein & Langer 1999; Woosley et al. 2002; Petermann et al. 2015; Choi et al. 2016).

Figure 7 shows the evolution of the central helium mass fraction, $X(^4He_c)$, during the core He-burning phase of the $20\,M_\odot$ models without mass loss. These central abundances, due to convective mixing, also represent the mass fraction values over the entire He-burning core. The core of these stars begin with $X(^4He_c) \approx 1$ and $X(^{16}O_c) \approx 0$ and, after $\approx 10^6$ yr, and end with $X(^4He_c) \approx 0$ and $X(^{16}O_c) \approx 0.8$, with the remainder being mostly ^{12}C.

The left panel of Figure 7 shows the evolution of $X(^4He_c)$ as a function of the number of isotopes in the nuclear reaction network, at a mass resolution of $\Delta M_{max} = 0.1\,M_\odot$ for the $M_{ZAMS} = 20\,M_\odot$ models without mass loss. The slopes of the lines shows the models are evolving at similar rates. The positive offset in the `mesa_204.net` is caused by the core being slightly cooler at the start of core helium convection, for the `approx22.net` the temperature is 177×10^6 K and for `mesa_204.net` it is 175×10^6 K. Nevertheless, the `mesa_204.net` model reaches $X(^4He_c) \approx 0$ at the same time as the other models. The spikes in $X(^4He_c)$ for the small `approx22.net`, expanded in the inset plot, are due to core breathing pulses (henceforth CBP, see Castellani et al. 1985). These occur when the $X(^4He_c)$ value is small such that if the core convection expands slightly outward in mass, then a small entrainment of unburnt ^4He leads to a large increase in the nuclear energy production (Straniero et al. 2003). For the `approx22.net` models, the edge of the convection core can move inwards and outwards $\approx 0.5\,M_\odot$ on timescales of ≈ 200 yr. The models with larger nuclear networks have significantly smaller CBPs as their convection cores move inwards and outwards $\approx 0.05\,M_\odot$, entraining a significantly smaller amount of additional ^4He fuel.

The left panel of Figure 7, shows that the `approx22.net` almost doubles $X(^4He_c)$ during a CBP. The nuclear energy generated from a CBP is sufficient to expand the stellar envelope as can be seen as a blue loop in theoretical HR diagrams (e.g., Constantino et al. 2016). The impact of a CBP is also mirrored in the evolution of $X(^{16}O_c)$, and leads to a larger $X(^{16}O_c)$ at the end of core He-burning and thus a smaller ^{12}C mass fraction. All these models at constant ΔM_{max} have between 1600-1700 zones and a similar timestep distribution at this evolutionary stage, thus the differences between CBPs are not due to changes in resolution. The presence of CBPs has been suspected as being a numerical artifact (Caputo et al. 1989; Boothroyd et al. 1993; Constantino et al. 2016), and we show that it can also be due to the choice of the nuclear network.

The right panel of Figure 7 shows the evolution of $X(^4He_c)$ as a function of mass resolution for `approx22.net`. There is a wide variation in $X(^4He_c)$. Both the $\Delta M_{max} = 0.1\,M_\odot$ and $\Delta M_{max} = 0.05\,M_\odot$ models have CBPs, with the $\Delta M_{max} = 0.05\,M_\odot$ models starting their CBPs at earlier times with a larger $X(^4He_c)$. This reinforces the notion that these `approx22.net` CBPs are purely numerical artifacts. Increasing the resolution above $\Delta M_{max} = 0.05\,M_\odot$ (which is also necessary for the ICZ to penetrate the H-core) is sufficient to prevent the CBP from forming. Models with CBPs have between 1500-2000 zones, while models without CBP have between 2000-7000 zones.

During core He-burning, the convective core grows, largely because the mass of the He-core itself grows from the overlying H-burning shell. This growth of the He-core has two effects. First, as the mass of the He-core grows so does the core luminosity, but the radius of the convective core stays nearly the same. This causes the density of the core to steadily increase as core He-burning proceeds. Second, as the mass of the He-core rises the ratio of the gas pressure to the total pressure decreases, which favors efficient convection in the core.

The core prior to C-ignition is composed of the ashes

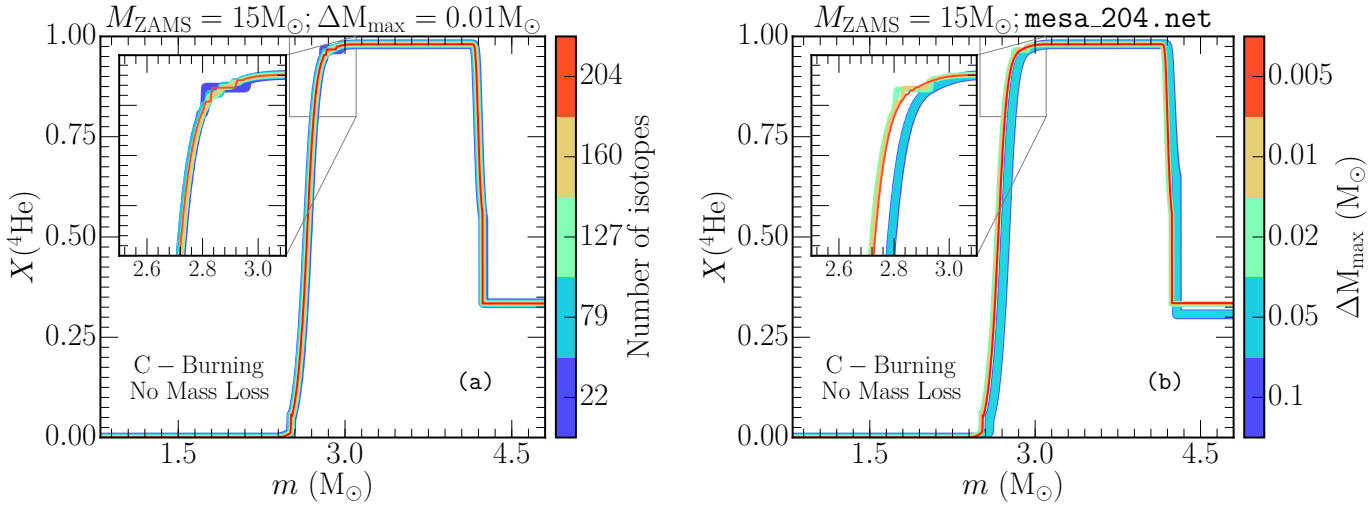

Figure 8. ^{4}He mass fraction profile at the onset of C-burning for the $M_{ZAMS} = 15\,M_\odot$ model without mass loss as a function of (a) the number of isotopes in the nuclear reaction network and (b) the mass resolution ΔM_{max}.

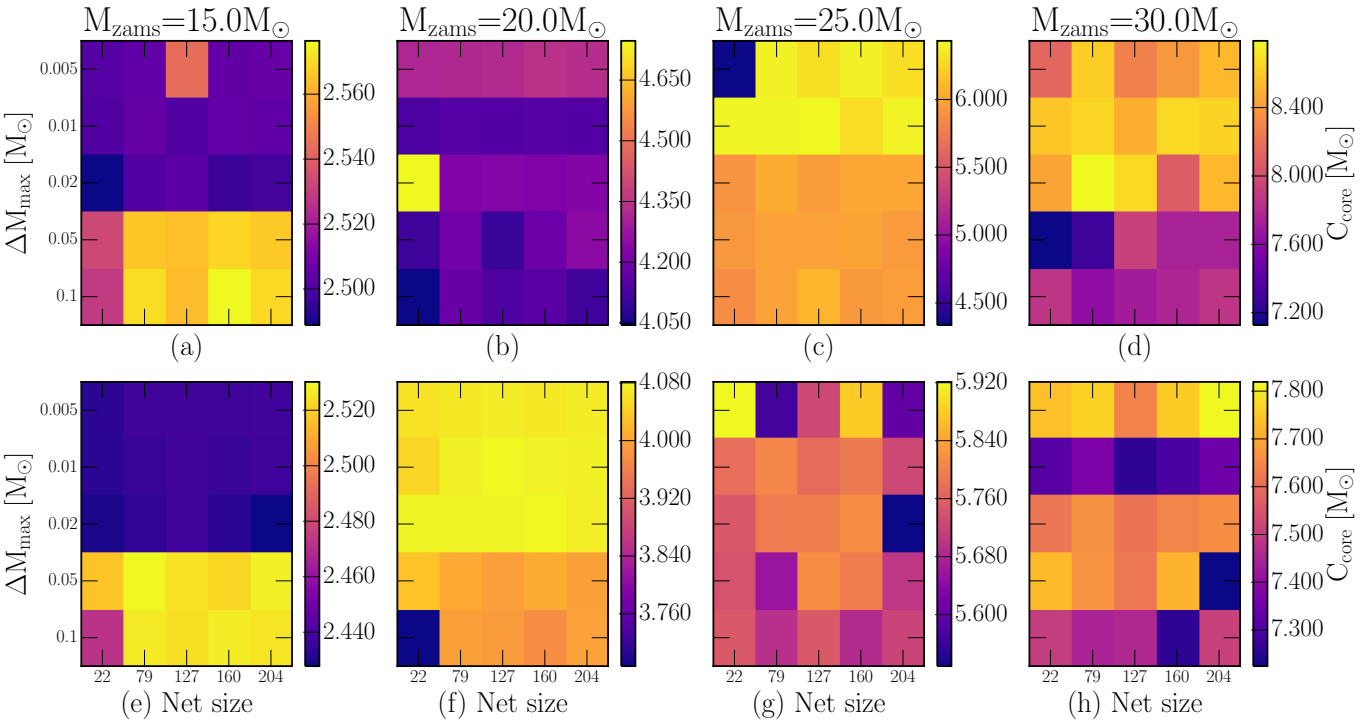

Figure 9. Carbon core mass at carbon ignition as a function of the number of isotopes in the network and mass resolution. Top: for MESA models without mass loss. Bottom: for models with mass loss.

of core He-burning, mainly ^{12}C and ^{16}O in a ≈1:4 ratio for the choice of $^{12}C(\alpha,\gamma)^{16}O$ reaction rate from the JINA reaclib version V2.0 2013-04-02 (see Figure 7, and West et al. 2013). There are also other isotopes present in trace amounts such as the neutron-rich ^{21,22}Ne, ^{25,26}Mg from processing the ashes of the CNO elements during He-burning; about 1% of X(^{20}Ne) from $^{16}O(\alpha,\gamma)^{20}$Ne during He-burning; the light s-process (which we do not follow); and other heavy elements present since the pre-MS from the initial composition.

Figure 8 shows the ^{4}He mass fraction profile during C-burning for a subset of the $M_{ZAMS} = 15\,M_\odot$ models. The left panel plots the X(^{4}He) profile as a function of the number of isotopes in the network for the models without mass loss and a mass resolution of $\Delta M_{max} = 0.01\,M_\odot$. The inset plot is a zoom in of the inner edge of the He-shell. We find the inner and outer mass location of the He-shell agree within ≈ ± $0.05\,M_\odot$ across all network sizes. The right panel plots the X(^{4}He) profile as a function of mass resolution for

the models without mass loss and that use the largest reaction network considered, `mesa_204.net`. The inset plot is a zoom of the inner edge of the He-shell. We find that mass resolutions of $\Delta M_{max} = 0.1$ and $0.05\,M_\odot$ do not sufficiently resolve the He-burning shell locations. For mass resolutions $\Delta M_{max} \lesssim 0.02\,M_\odot$ we find convergence of the He-shell inner and outer boundaries.

3.4. *C-burning*

Figure 9 shows the C-core mass at the onset of C-burning as a function of mass resolution and the number of isotopes in the nuclear reaction network. The core mass is defined as the mass location where $X(^{12}C) > 0.1$ and $X(^4He) < 0.01$, measured when the core reaches $\log_{10}(T_c/K) = 8.95$. These maps share many of the same variations, chiefly the bifurcations and outliers, that are inherited from core H-burning (see Figure 5). For the $M_{ZAMS} = 15\,M_\odot$ models without mass loss the initial C-core mass is in the range ≈ 2.49–$2.57\,M_\odot$, while models with mass loss span ≈ 2.43–$2.52\,M_\odot$. For the $M_{ZAMS} = 20\,M_\odot$ models without mass loss have initial C-core masses spanning ≈ 4.0–$4.3\,M_\odot$, while models with mass loss span ≈ 3.9–$4.1\,M_\odot$. Our $M_{ZAMS} = 25\,M_\odot$ models without mass loss show initial C-core masses of ≈ 5.7–$6.3\,M_\odot$, while models with mass loss span ≈ 5.6–$5.8\,M_\odot$. The $M_{ZAMS} = 30\,M_\odot$ models without mass loss have an initial C-core mass range of ≈ 7.8–$8.7\,M_\odot$, while models with mass loss span ≈ 7.3–$7.8\,M_\odot$.

Comparing with Figure 6, the $M_{ZAMS} = 15\,M_\odot$ models with initially more massive He-core have less massive C-cores at carbon ignition. This is due to less massive ZAMS models having a larger electron degeneracy in the C-core, a larger ρ_c, and thus an enhanced screening factor for the $^{12}C+^{12}C$ reaction rate. For models more massive than the $M_{ZAMS} = 15\,M_\odot$, those with larger He-cores have the largest C-core at carbon ignition.

All the $M_{ZAMS} = 15\,M_\odot$ models undergo convective C-ignition at the center of the star followed by a series of 3 convective flashes, where each additional flash ignites at the approximate maximum mass location of the previous convective C-flash. All the $M_{ZAMS} = 25\,M_\odot$ and $30\,M_\odot$ models show C-ignition under radiative conditions that propagates outwards in mass, followed by a single convective flash. The $M_{ZAMS} = 20\,M_\odot$ models have a more complex C-ignition that straddles the boundary between radiative and convective carbon burning (Timmes et al. 1996; Heger et al. 2000; Hirschi et al. 2004).

Figure 10 shows the differences in core C-ignition for the $M_{ZAMS} = 20\,M_\odot$ model without mass loss and with the `mesa_160.net` network. As the mass resolution increases, C-ignition transitions from radiative conditions at the coarsest resolution ($\Delta M_{max} = 0.1\,M_\odot$) to a mixture of convective and radiative conditions at intermediate resolutions ($\Delta M_{max} = 0.05\,M_\odot$), and finally to purely convective conditions at higher resolutions ($\Delta M_{max} = 0.02\,M_\odot$). Models with yet finer mass resolution are similar to the $\Delta M_{max} = 0.02\,M_\odot$ case.

Carbon burning in all cases begins at the center. In the case of the $M_{ZAMS} = 20\,M_\odot$ model with the coarsest resolution shown in Figure 10, the central temperature is large enough ($T_{9,c} \approx 0.8$) to burn carbon despite the central regions still being dominated by thermal neutrino cooling (light purple). Only near $M \approx 0.3\,M_\odot$ at $\log_{10}((\tau_{cc} - \tau)/yr) \approx 1.7$ does the nuclear energy generation rate from burning overtake the thermal neutrino cooling rate, and thus the color in the Kippenhahn transitions to red.

As the C-ignition conditions transition from radiative to convective, the time spent in the core C-burning phase increases from ≈ 45 yr to ≈ 250yr. After carbon burning ceases, the star has ≈ 1 year until core-collapse. As the mass resolution increases the mass location of the innermost boundary of the ^{4}He shell (see Figure 8) decreases, while the mass location of the outer boundary of the ^{12}C shell increases, by $\approx 0.03\,M_\odot$. In addition, as the resolution increases $\log_{10}(T_c/K)$ decreases from 8.90 to 8.88 and $\log_{10}(\rho_c/(g\ cm^{-3}))$ decreases from 5.36 to 5.20. The combustion at the top of the final carbon flash is predominantly neutron captures, with the neutrons provided by ^{22}Ne, onto the ashes of C-burning to form ^{23}Na,^{25,26}Mg and ^{27}Al.

Figure 11 shows the mass fraction profiles at core C-depletion for the $M_{ZAMS} = 20\,M_\odot$ model with mass loss, $\Delta M_{max} = 0.01\,M_\odot$, and the `mesa_204.net` reaction network. The composition of the core prior to Ne-ignition is the ashes of core C-burning, mainly ^{16}O, ^{20,21}Ne, ^{23}Na, ^{24,25,26}Mg, ^{26,27}Al, to a smaller extent ^{29,30}Si, ^{31}P, and other heavy elements present since the pre-MS from the initial composition and from any s-processing during helium burning (Arnett & Truran 1969; Arnett 1972a; Endal 1975; Lamb et al. 1976; Arnett & Thielemann 1985; Woosley & Weaver 1995; Woosley et al. 2002; Hirschi et al. 2004; Bennett et al. 2012).

Carbon is not completely destroyed, as would be expected for complete combustion, due to the short amount of time the final convective flash lasts. The initial flashes in Figure 10 last tens or hundreds of years depending on resolution and number of isotopes in the reaction network. The final flash lasts only a few years, which is insufficient to burn all the carbon over the approximately few solar masses the final convection zone covers. The flash does not survive longer due to the convection being driven by the burning at the base of the convection zone. This burning front attempts to propagate towards the central regions, but encounters the ashes from the previous flash. This ash has insuffi-

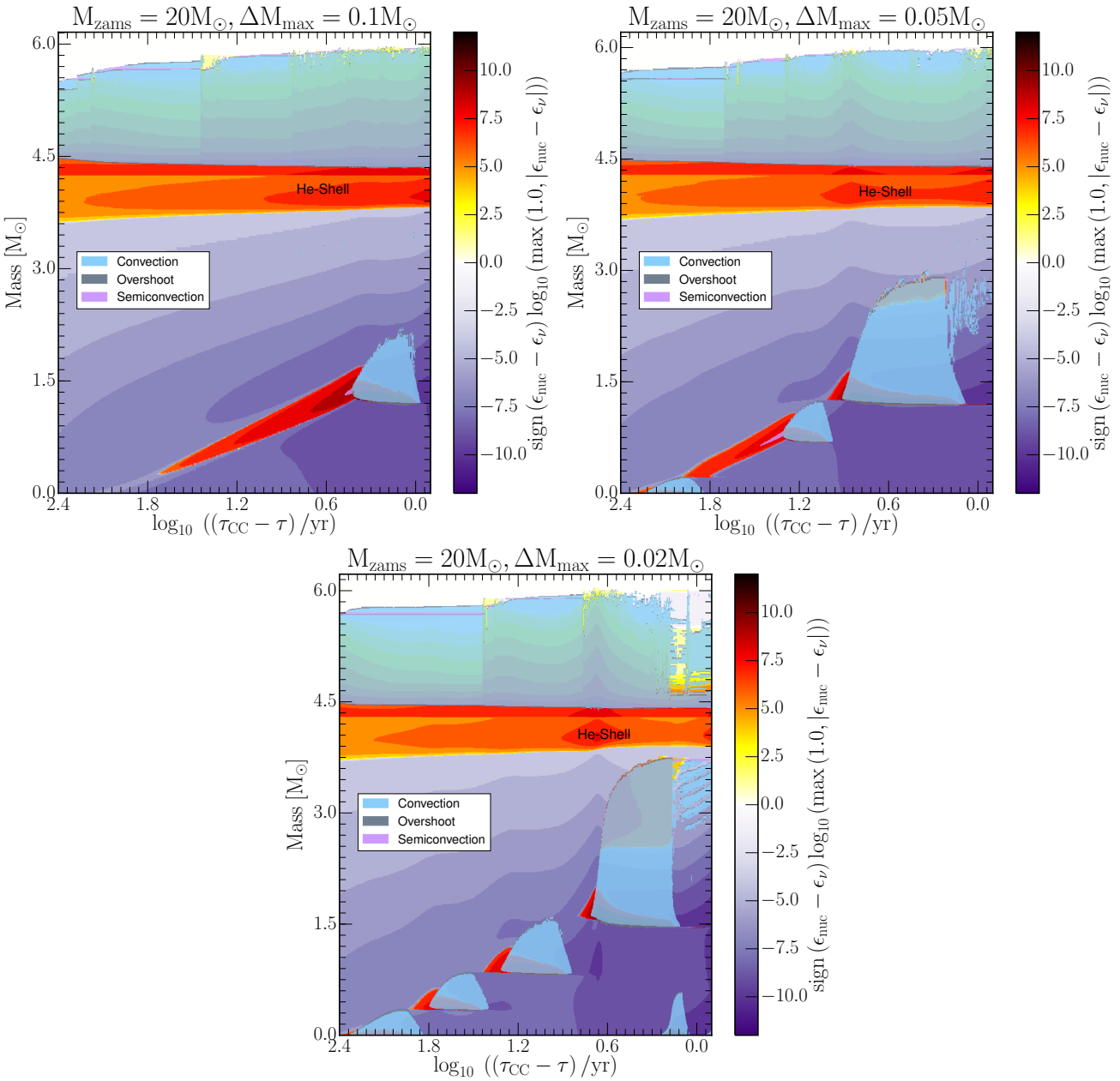

Figure 10. Kippenhahn plots for the $M_{ZAMS} = 20\,M_\odot$ models without mass loss and the `mesa_160.net` reaction network. Top left, $\Delta M_{max} = 0.1\,M_\odot$; Top right, $\Delta M_{max} = 0.05\,M_\odot$; Bottom, $\Delta M_{max} = 0.02\,M_\odot$. Time is measured in years until core-collapse. Red/orange regions denote vigorous burning, while purple denotes significant cooling and electron degeneracy. Light blue are regions with convection, grey regions with convective overshoot and purple regions with semiconvection, thermohaline mixing is not shown for clarity. At the coarsest resolution (top left) carbon burns under radiative condition with one convective episode. At finer resolution (top right) carbon ignites under radiative/convective conditions followed by two convective flashes, while at the higher resolutions (bottom), C-ignition occurs under convective conditions with three episodes of convective C-burning.

cient ^{12}C to sustain the proto-flame and the convection dies. The situation has similarities to C-burning flames in Super Asymptotic Giant Branch models (Denissenkov et al. 2013; Chen et al. 2014; Farmer et al. 2015). The carbon left behind is thus predominantly concentrated at the top of the CO core, and may ignite again as a carbon shell (see Figure 18).

3.5. *Ne-burning*

Neon is the next abundant nucleus to burn in balanced power via the $^{20}\mathrm{Ne}(\gamma,\alpha)^{16}\mathrm{O}$ photodisintegration reaction (Arnett 1974) at a core temperature of $T_9 \approx 1.5$ and core density of $\log_{10}\rho \approx 6.6$ g cm^{-3}. The net result is that $2(^{20}\mathrm{Ne}) \rightarrow {}^{16}\mathrm{O} + {}^{24}\mathrm{Mg}$ at a rate determined by how fast ^{20}Ne captures α-particles from the equilibrium set up between ^{16}O and ^{20}Ne (e.g., Busso & Gallino 1985; Thielemann & Arnett 1985; Chieffi et al. 1998; Woosley et al. 2002).

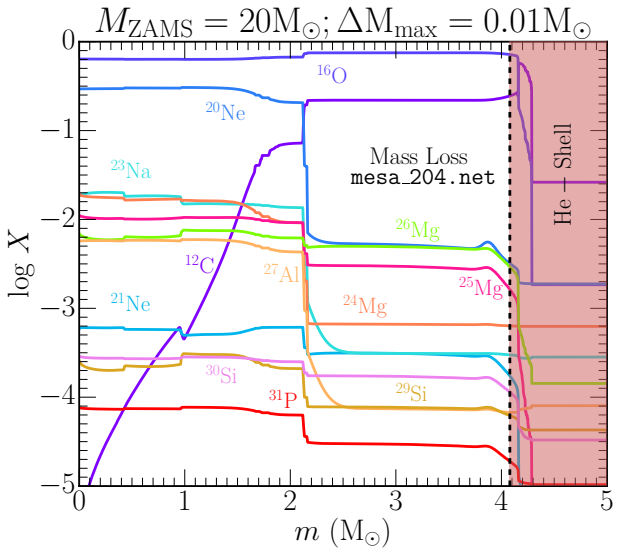

Figure 11. Mass fraction profiles at core C-depletion for the $M_{ZAMS} = 20\,M_\odot$ model with $\Delta M_{max} = 0.01\,M_\odot$, `mesa_204.net`, and mass loss. The corresponding evolutionary time is $\log_{10}((\tau_{cc} - \tau)/{\rm yr}) \approx 0.48$.

For the $M_{ZAMS} = 15\,M_\odot$ models, Ne-ignition occurs predominately at the center which drives a $\approx 0.5\,M_\odot$ convection zone for approximately one month. As M_{ZAMS} increases to 20 and $25\,M_\odot$, this initial Ne-flash can be followed by a subsequent Ne-flash which may or may not drive a convective region once O-burning has become vigorous. For the $M_{ZAMS} = 30\,M_\odot$ models the initial Ne-flash is followed by one or more additional Ne-flashes which propagate outwards in mass to $\approx 1\,M_\odot$.

Figure 12 shows a variety of Ne-burning behaviors for the $M_{ZAMS} = 30\,M_\odot$ models with mass loss. The model using the `approx22.net` reaction network (upper left) shows a series of outward moving convective flashes starting at $\log_{10}((\tau_{cc} - \tau)/{\rm yr}) = -0.2$ and ending at $\log_{10}((\tau_{cc} - \tau)/{\rm yr}) = -0.8$. The model using the `mesa_127.net` reaction network (upper right) shows neon ignites in a weak radiative flash, that lasts ≈ 1 month. For the `mesa_160.net` model (lower left) there is an extensive off-center radiative burning region which transitions into a convective flash. Finally, the `mesa_204.net` model contains a series of off-center flashes, where a pocket of convection persists from the first ignition of neon to the ignition of oxygen.

Figure 13 shows the evolution of T_c and ρ_c for the models shown in Figure 12. The $M_{ZAMS} = 30\,M_\odot$ models start Ne-burning at $\log_{10}({\rm T/K}) \approx 9.17$ and $\log_{10}(\rho_c/({\rm g\,cm^{-3}})) \approx 6.6$. As Ne-burning progresses the density and temperature increase until core O-burning begins with an accompanying creation of a central convection zone which lowers ρ_c. The tracks are well converged. The maximum temperature difference is from $T_{9,c} \approx 1.65$ to ≈ 1.50, a $\approx 8\%$ difference, with the largest offset in the `approx22.net`. As the number of isotopes in the reaction network increases, the core is denser for a given temperature. The larger networks thus undergo increased neutrino cooling, which is density dependent but not dependent on the isotopes in the network. This increased cooling rate is what prevents the neon from vigorously igniting at the center, and prevents the ignition from driving a central convection zone.

These variations in burning structure due to changes in the number of isotopes in the nuclear reaction network lead to variations in the post Ne-burning abundance profiles. For the $M_{ZAMS} = 30\,M_\odot$ models in Figure 12, the `approx22.net` model burns neon the longest amount of time and over the most mass, and thus shows the largest abundance changes. We find $X(^{24}{\rm Mg})$ is enhanced by a factor ≈ 6 compared to the pre-Ne burning mass fraction. Models with the softwired `mesa_127.net`, `mesa_160.net`, `mesa_204.net` networks, show an $X(^{24}{\rm Mg})$ enhancement factor that increases as the number of isotopes increases; from ≈ 1.5 for the `mesa_127.net` model to ≈ 2.0 for the `mesa_204.net` model, with the a total of $\approx 0.05\%$ $X(^{24}{\rm Mg})$ left. The other main product of Ne-burning, ^{16}O, increases from ≈ 0.7 to ≈ 0.8 in the inner $1.5\,M_\odot$, with the relative change increasing as the number of isotopes increases similar to the ^{24}Mg.

3.6. *O-burning*

The large ^{16}O mass fraction, coupled with $^{16}{\rm O}+^{16}{\rm O}$ being a true fusion reaction and not a photodisintegration driven event like Ne-burning or Si-burning, ensures that O-burning is a key energetic and nucleosynthesis stage in the late phases of massive star evolution (Rakavy et al. 1967; Arnett 1972b; Woosley et al. 1972; Woosley & Weaver 1995; El Eid et al. 2004; Sukhbold et al. 2016).

In 1D stellar evolution instruments such as `MESA`, convective mixing and energy transport is modeled using MLT in a time dependent manner (Vitense 1953; Böhm-Vitense 1958; Cox & Giuli 1968), which is usually tuned to reproduce solar properties (Asplund et al. 2009). However, thermal neutrino cooling speeds up O-burning to such an extent that the evolutionary timescales are close to the sound crossing time, so that direct, multi-dimensional compressible numerical hydrodynamics must be applied for maximum fidelity to the underlying physics. Such studies show nuclear burning tightly couples to turbulent convection so that fuel is consumed in chaotic episodes (Bazán & Arnett 1998; Asida & Arnett 2000; Meakin & Arnett 2007a). Core O-burning and shell O-burning are dominated by large scale modes of fluid flow, which are of such low order that they do not cancel to a smooth spherical behavior (Couch et al. 2015; Chatzopoulos et al. 2016; Jones et al. 2016; Müller et al. 2016). Moreover, 3D simulations of

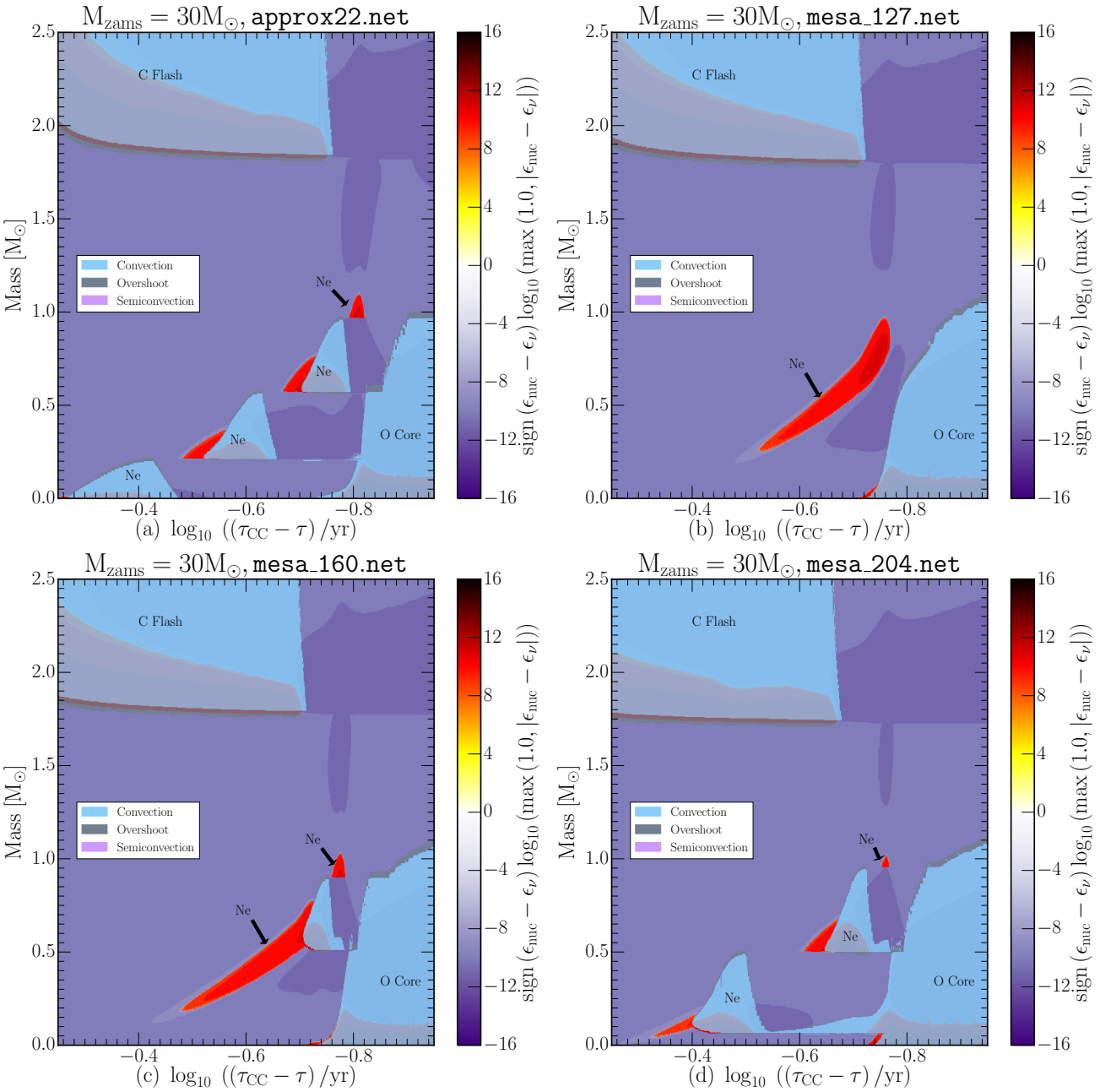

Figure 12. Core Ne-burning Kippenhahn plots of the $M_{ZAMS} = 30\,M_\odot$ models with mass loss and $\Delta M_{max} = 0.01\,M_\odot$ for different nuclear reaction networks. Top left (a), `approx22.net`; Top right (b), `mesa_127.net`; Bottom left (c), `mesa_160.net`; Bottom right (d), `mesa_204.net`. Time is measured in years until core-collapse.

O-burning suggest that MLT gives an incomplete representation of stellar convection (Arnett et al. 2015). Nevertheless, 3D simulations of core O-burning and beyond are resource intensive and to date have been run primarily to address hydrodynamic and transport aspects. Such 3D simulations have not yet been run to assess the detailed nucleosynthesis.

Figure 14 shows the O-core masses at the start of core oxygen convection. We define this as the location where $X(^{16}O) > 0.1$ and $X(^{12}C) < 0.01$ and measured when $X(^{16}O_c) = 0.7$. In general, as the mass resolution increases the O-core mass decreases, with the $M_{ZAMS} = 15\,M_\odot$ models having the smallest spread. This is due to the $15\,M_\odot$ models having a more consistent behavior between the start of carbon and the end of neon burning. The O-core masses range from $1.35-1.4\,M_\odot$ for the $15\,M_\odot$ models, $1.5-2.5\,M_\odot$ for the $M_{ZAMS} = 20\,M_\odot$ models, $1.8-3.0\,M_\odot$ for the $25\,M_\odot$, and $2.25-3.15\,M_\odot$ for the $M_{ZAMS} = 30\,M_\odot$ models. The spread in the O-core mass is smaller for the mass losing models compared to models without mass loss. Much of the fine structure seen in Figures 6 and 9 has

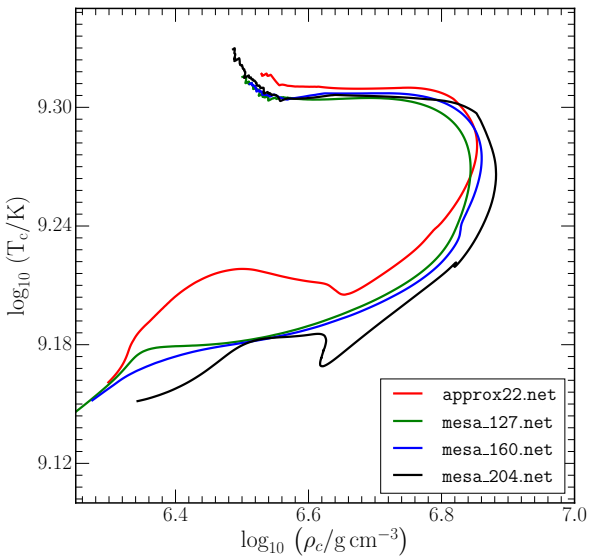

Figure 13. Evolution of the central temperature and density for the $M_{ZAMS} = 30\,M_\odot$ models shown in Figure 12.

been erased due to the variations in carbon and neon burning. Panels (e) and (f) still show a clear bifurcation however, with the lowest resolution models having the largest O-core masses.

Figure 15 shows the evolution during core O-burning for the $M_{ZAMS} = 15\,M_\odot$ models without mass loss, the `mesa_204.net` reaction network, and mass resolutions of $\Delta M_{max} = 0.1\,M_\odot$, $0.02\,M_\odot$, and $0.005\,M_\odot$. In each model O-ignition occurs at the center at $\log_{10}((\tau_{cc} - \tau)/yr) \approx 0.4$ and O-burning continues until $\log_{10}((\tau_{cc} - \tau)/yr) \approx -0.5$. O-burning is concentrated over $\approx 0.1\,M_\odot$ of the core, while a convective region is generated out to $\approx 1.0\,M_\odot$. For $\Delta M_{max} = 0.1\,M_\odot$, the convective region undergoes a series of contractions and expansions (in mass coordinates), analogous to the CBP seen during core He-burning. During a core oxygen breathing pulse (OBP), when the convective region reaches its maximum extent (in mass coordinate) and ingests ^{16}O, there is a brief increase in the extent of the central burning region and a corresponding increase in the energy released in the core. These OBPs have a smaller effect on the ^{16}O abundance compared to CBPs, due to the weaker density dependency of O-burning compared to He-burning. These OBPs are present for all four masses considered in this work and unlike the helium counterparts these OBPs are independent of the nuclear network used. As the mass resolution increases the OBP behavior changes, the number of OBPs decreases, the maximum mass the OBPs extend out to decreases, and they have a shorter lifetime. This suggests careful treatment of the mass resolution is needed during this stage of a star's evolution.

Once core O-burning ceases the core contracts until Si-ignition. During this contraction phase the $M_{ZAMS} = 15\,M_\odot$ models undergo a series of off-center flashes. These mimic the ignition at the center by having a series of small neon flashes which lead to a larger oxygen flash. The residual carbon left behind from carbon burning (Figure 11) can also now ignite as an additional flash near the edge of the CO core. For the $M_{ZAMS} = 15\,M_\odot$ models in Figure 15, as the numerical resolution increases the number of these flashes decreases, the $\Delta M_{max} = 0.1\,M_\odot$ has three oxygen flashes and a number of smaller neon flashes, while the $\Delta M_{max} = 0.02\,M_\odot$ and $\Delta M_{max} = 0.005\,M_\odot$ has only one oxygen flash and a variable number of neon flashes. As the initial mass of the star increases the number of neon/oxygen flashes decreases and the carbon flash ignites later, once silicon burning has commenced.

Dominating the ashes of O-burning are Si, S, Ar, Ca in roughly solar proportions. Figure 16 shows the isotopes ^{28}Si, ^{32,33,34}S, ^{35,37}Cl, ^{36,38}Ar, ^{39,41}K, and ^{40,42}Ca are present in significant quantities (e.g., Woosley & Weaver 1995; Limongi et al. 2000; Limongi & Chieffi 2003; Sukhbold et al. 2016) for the $M_{ZAMS} = 15\,M_\odot$ model with mass loss and $\Delta M_{max} = 0.01\,M_\odot$. During O-burning several isotopes begin to be made as radioactive progenitors of stable isotopes, for example, ^{37}Cl as ^{36}Ar and ^{41}K as ^{41}Ca. The heaviest isotopes ($A \gg 50$) that were present in the initial composition at birth, along those heavy isotopes made from the s-process during He-burning and C-burning (which we do not follow), begin to be destroyed by photodisintegration reactions; essentially melting them into the Fe-group. O-burning also features the first appearance of quasi-equilibrium clusters (Bodansky et al. 1968; Woosley et al. 1973; Woosley & Hoffman 1992; Hix & Thielemann 1996; Meyer et al. 1998). These clusters grow to encompass more isotopes as core O-burning proceeds. Weak interactions such as ^{33}S$(e^-,\nu_e)^{33}$P, $^{35}35(e^-,\nu_e)^{35}$S, and ^{37}Ar$(e^-,\nu_e)^{37}$Cl decrease the Y_e significantly during O-burning, especially at O-depletion (e.g., Heger et al. 2001). For example, we find $Y_{e,c} \approx 0.4778$ at core O-depletion for the model shown in Figure 16, which has decreased from $Y_{e,c} = 0.499$ prior to O-burning.

3.7. *Si-burning*

Silicon burning is the last exothermic burning stage and produces the Fe-peak nuclei. Due to Coulomb repulsion, it is improbable that two ^{28}Si nuclei will fuse to ^{56}Ni. Instead, a photodisintegration driven rearrangement of the abundances takes place, originating from equilibria established among individual reactions with their reverse reactions (Bodansky et al. 1968). When such equilibria happen among many reactions, the material reaches an equilibrium state where nuclei merge

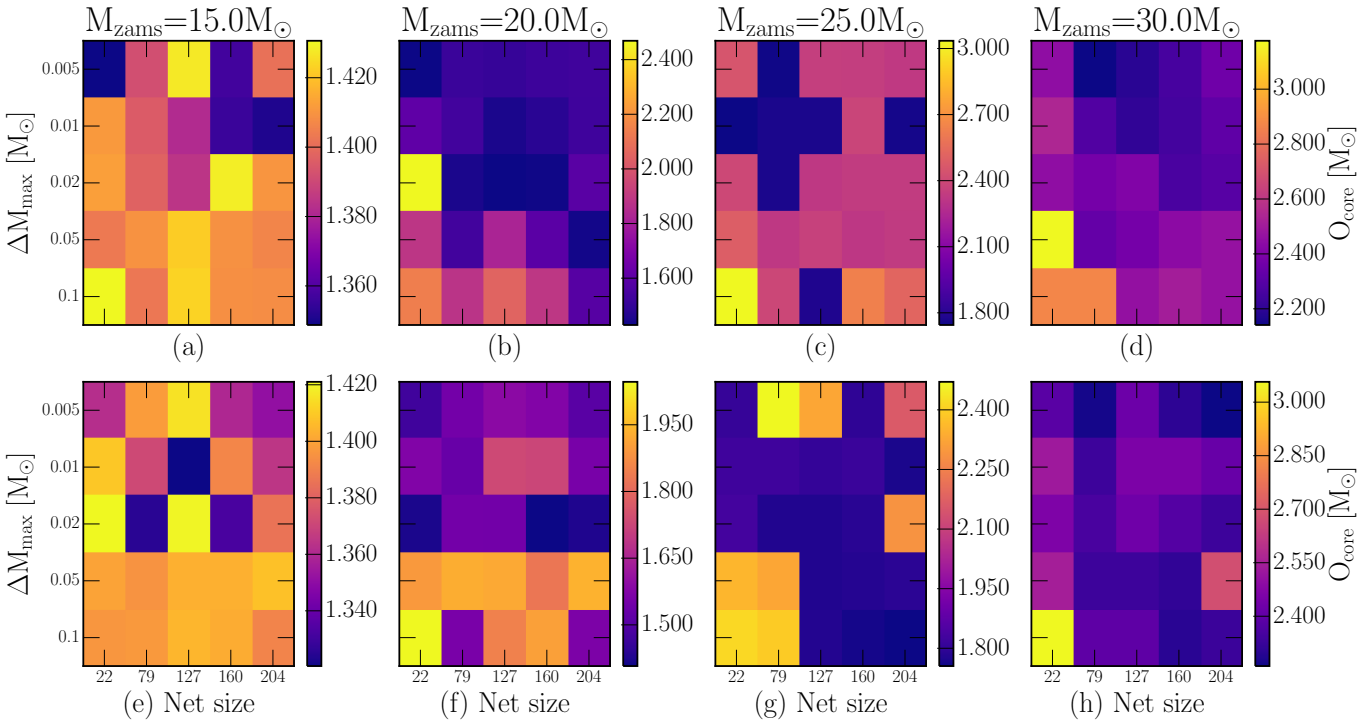

Figure 14. Oxygen core mass at oxygen ignition, defined when $X(^{16}O_c) = 0.7$, as a function of the number of isotopes in the reaction network and mass resolution. Top: for `MESA` models without mass loss. Bottom: with mass loss.

into clusters. Units of interaction are no longer nuclei, but the clusters themselves, which adapt their properties according to the local thermodynamic conditions (Woosley et al. 1973; Woosley & Hoffman 1992; Hix & Thielemann 1996; Meyer et al. 1998; The et al. 1998; Hix & Thielemann 1999; Magkotsios et al. 2010).

In general, not all reactions are in equilibrium. Consequently, this state is named quasi-static equilibrium (QSE). The special case where all strong and electromagnetic reactions are balanced by their reverse reactions is called nuclear statistical equilibrium (NSE), because all mass fractions may be described in terms of statistical properties of excited nuclear states (e.g., temperature dependent partition functions) and nuclear structure variables (masses and Q values; Clifford & Tayler 1965; Hartmann et al. 1985; Nadyozhin & Yudin 2004; Jordan & Meyer 2004; Seitenzahl et al. 2008).

Weak interactions are excluded from these definitions since for conditions relevant to hadronic physics, they never attain equilibrium (e.g., Heger et al. 2001; Arcones et al. 2010). Hence, equilibrium notions are related only with strong and electromagnetic interactions. In practice, there is either one cluster in NSE or QSE, or two QSE clusters, one for the Si-group and one for the Fe-group nuclei. Even the main products of Si-burning depend quite sensitively on small changes of the electron fraction, temperature and density. Although the physics of QSE/NSE is relevant for our models, we reiterate that no QSE or NSE approximations are made in our models.

During Si-burning, as for O-burning, the energetics of nuclear burning tightly couples to turbulent convection, and must be modeled with 3D simulations to assess the fidelity of the approximations made by 1D stellar evolution instruments (e.g., Arnett & Meakin 2011; Couch et al. 2015; Müller et al. 2016; Jones et al. 2016). For example, Couch et al. (2015) found that during the final minutes of Si-burning in a massive star that the fluctuating, peak convective speeds of $\approx$ 200 km s^{-1} were common and that the speed of the convection increases to $\approx$ 500 km s^{-1} as collapse approaches and the core contracts. These speeds are not negligible relative to nominal infall speeds of 1000 km s^{-1} for our core-collapse initial models. Distilling the essential features of 3D simulations into models suitable for 1D stellar evolution instruments remains a challenge for future investigations.

Figure 17 shows the Si-core mass at Si-ignition. This is defined as the location where $X(^{28}Si) > 0.1$ and $X(^{16}O) < 0.01$, measured when $\log_{10}(T_c/K) = 9.5$. As the mass resolution increases there is a general trend, with substantial scatter, for the Si-core mass to decrease, with the $M_{ZAMS} = 15\,M_\odot$ and $20\,M_\odot$ models having the smallest spread. The Si-core masses range from $1.05 - 1.35\,M_\odot$ for the $15\,M_\odot$ models, $1.3 - 1.6\,M_\odot$ for the $M_{ZAMS} = 20\,M_\odot$ models, $1.0 - 1.7\,M_\odot$ for the $25\,M_\odot$ models, and $1.1 - 1.6\,M_\odot$ for the $M_{ZAMS} = 30\,M_\odot$ models. The spread in the Si-core mass is about the same

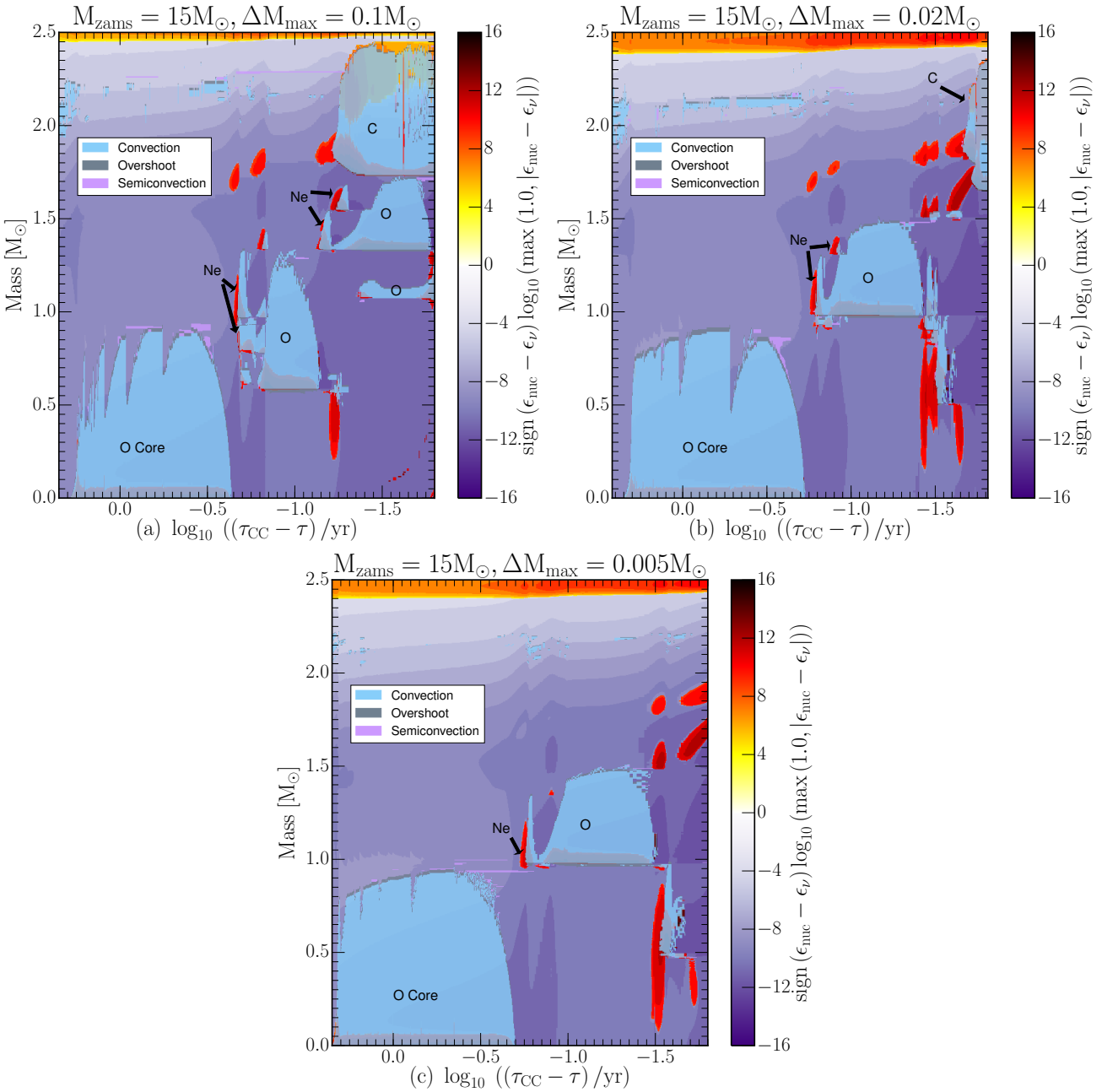

Figure 15. Core O-burning Kippenhan plots of the $M_{ZAMS} = 15\,M_\odot$ models without mass loss and `mesa_204.net` with various ΔM_{max}. Top left (a), ΔM_{max}=0.1; Top right (b), ΔM_{max}=0.02; Bottom (c), ΔM_{max}=0.005. Time is measured in years until core-collapse. Fuels driving selected radiative or convective regions are labeled.

for the mass losing models compared to models without mass loss. Nearly all of the fine structure seen in Figures 6 and 9, and even the coarser structure in Figure 14, has been largely erased before the onset of Si-burning. The bulk of the silicon core is built during the core oxygen burning phase, but a number of short flashes, which can be seen in Figure 15 at $\log_{10}((\tau_{cc} - \tau)/\mathrm{yr}) \approx -1.5$, can occur before core Si-burning commences. These flashes introduce an additional fine structure into the core composition and hence the location of the silicon core boundary.

Figure 18 shows the evolution during core Si-burning for $M_{ZAMS} = 25\,M_\odot$ models with mass loss and $\Delta M_{max} = 0.005\,M_\odot$ for the `approx22.net`, `mesa_160.net` and `mesa_204.net` reaction networks. Silicon ignites at the center within one day of core-collapse. The initial phase of transforming ^{28}Si is sensitive to the thermodynamic conditions and electron captures change the Y_e continuously during the buildup of the QSE clusters (e.g., Thielemann & Arnett 1985).

For the `approx22.net` model in Figure 18, Si-burning propagates outwards to $\approx 1\,M_\odot$ driving a convection

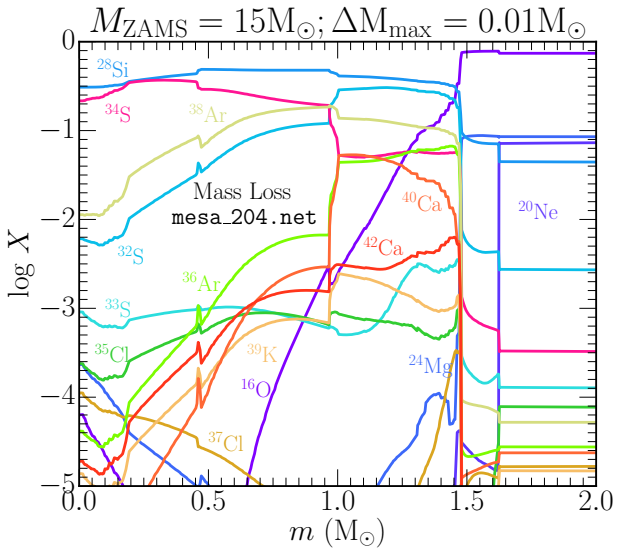

Figure 16. Mass fraction profiles of abundant isotopes at core O-depletion for the $M_{ZAMS} = 15\,M_\odot$ model with $\Delta M_{max} = 0.01\,M_\odot$, `mesa_204.net`, and mass loss. The corresponding evolutionary time is $\log_{10}((\tau_{cc} - \tau)/\mathrm{yr}) \approx -1.95$.

region over this mass range. The Si-burning region then recedes to $\approx 0.5\,M_\odot$ while leaving the convection zone behind. For the models using the `mesa_160.net` and `mesa_204.net` reaction networks there is a central burning region occupying $\approx 0.2\,M_\odot$. Outside this core region is a mixed region comprised of many small pockets of radiative/convective burning. The larger and more simply-connected convective region for the `approx22.net` allows a larger fraction of the ^{28}Si to be converted into iron-group elements and to homogenize the spatial distribution of those iron-group isotopes. The final Y_e in the `mesa_160.net` and `mesa_204.net` models is determined to within $\approx 2\%$ before the iron-core begins to collapse, making shell Si-burning a key evolutionary state for determining the $Y_{e,c}$ and the iron-core structure (e.g., Heger et al. 2001).

Figure 18 also shows a change in the qualitative behavior of the carbon shell. Carbon burns at the base of a convective region in the $M_{ZAMS} = 25\,M_\odot$ models using the `approx22.net` reaction network, at $\approx 3.0\,M_\odot$ and $\log_{10}((\tau_{cc} - \tau)/\mathrm{yr}) \geq -2.25$, and has been since core O-burning. In contrast, the models using the `mesa_160.net` reaction network show C-burning in two distinct layers, one layer at $\approx 2.0\,M_\odot$ and a second layer at $\approx 2.4\,M_\odot$, once Si-burning becomes vigorous. The $M_{ZAMS} = 25\,M_\odot$ models using the `mesa_204.net` reaction network do not ignite a carbon shell, chiefly due to an oxygen flash at $\approx 1.5\,M_\odot$ and $\log_{10}((\tau_{cc} - \tau)/\mathrm{yr}) = -2.25$ where a previous convection region extended out to $\approx 5\,M_\odot$. This region partially burnt C, Ne, and O leaving behind the mixed convection/semiconvection due to small scale composition gradients, as seen in Figure 18 for `mesa_204.net`.

Figure 19 shows the composition of the cores at $\log_{10}((\tau_{cc} - \tau)/\mathrm{yr}) = -3.0$ for the $M_{ZAMS} = 25\,M_\odot$ models in Figure 18. The left panel corresponds to the stellar model using the `approx22.net` reaction network and the right panel corresponds to the models using the `mesa_204.net` reaction network. First, we note that the `approx22.net` model has a significantly smoother composition profiles in the inner $\approx 1.5\,M_\odot$ due to the more simply connected convective region it exhibits (see Figure 18) relative to the multiple-connected convective regions exhibited by the `mesa_204.net` model. Second, the core in the `approx22.net` model is predominately ^{54}Fe, while at the same time until core-collapse the `mesa_204.net` model is a mix of ^{54,56}Fe and ^{52}Cr. At the center of the `mesa_204.net` model the composition is $\approx 68\%$ ^{56}Fe, $\approx 18\%$ ^{52}Cr and $\approx 2\%$ ^{54}Fe, with the remainder in various iron group elements. Third, there is a significant impact of the different shell O-burning behavior in the 2-5 $M_\odot$ range, before silicon burning commences (see Figure 18). The model using the `mesa_204.net` reaction network has a smaller ^{16}O mass fraction that extends deeper into the core than the model using the `approx22.net` reaction network. The O shell has also been polluted by the products of oxygen burning as well as being depleted in ^{12}C.

3.8. *Core-Collapse*

When the Fe-core reaches its finite-temperature Chandrasekhar mass (Baron & Cooperstein 1990),

$$M_{\rm Ch,eff} \simeq 5.76\, Y_e^2 \times \left[1 - 0.057 + \left(\frac{s_e}{\pi Y_e}\right)^2 + 1.21\left(\frac{s_e}{A}\right)\right]\ M_\odot, \quad (4)$$

electron capture and photodisintegration drive the collapse of the Fe-core with the largest infall speeds being reached near the outer edge of the Fe-core. Here, $s_e = S_e/(N_A k)$ is a dimensionless average electron entropy and A is an average atomic weight. We terminate our `MESA` models when any mass coordinate within the Fe-core exceeds an inward velocity of 1000 km s^{-1}. The structural and nucleosynthesis properties at this key evolutionary point (e.g., Woosley & Weaver 1995; Hirschi et al. 2004; Dessart et al. 2010; Chieffi & Limongi 2013) can have significant effects on the subsequent explosion (if achieved) and nucleosynthesis (e.g. Janka 2012; Dolence et al. 2013; Ott et al. 2013; Couch & O'Connor 2014; Pejcha & Thompson 2015; Couch et al. 2015; Müller et al. 2016; Jones et al. 2016; Bruenn et al. 2016).

Figure 20 shows the final Fe-core mass (which we define below) at core-collapse,taken when the radial infall speed reaches $v > 1000$ km s^{-1}, as a function of the mass resolution ΔM_{max} and the number of iso-

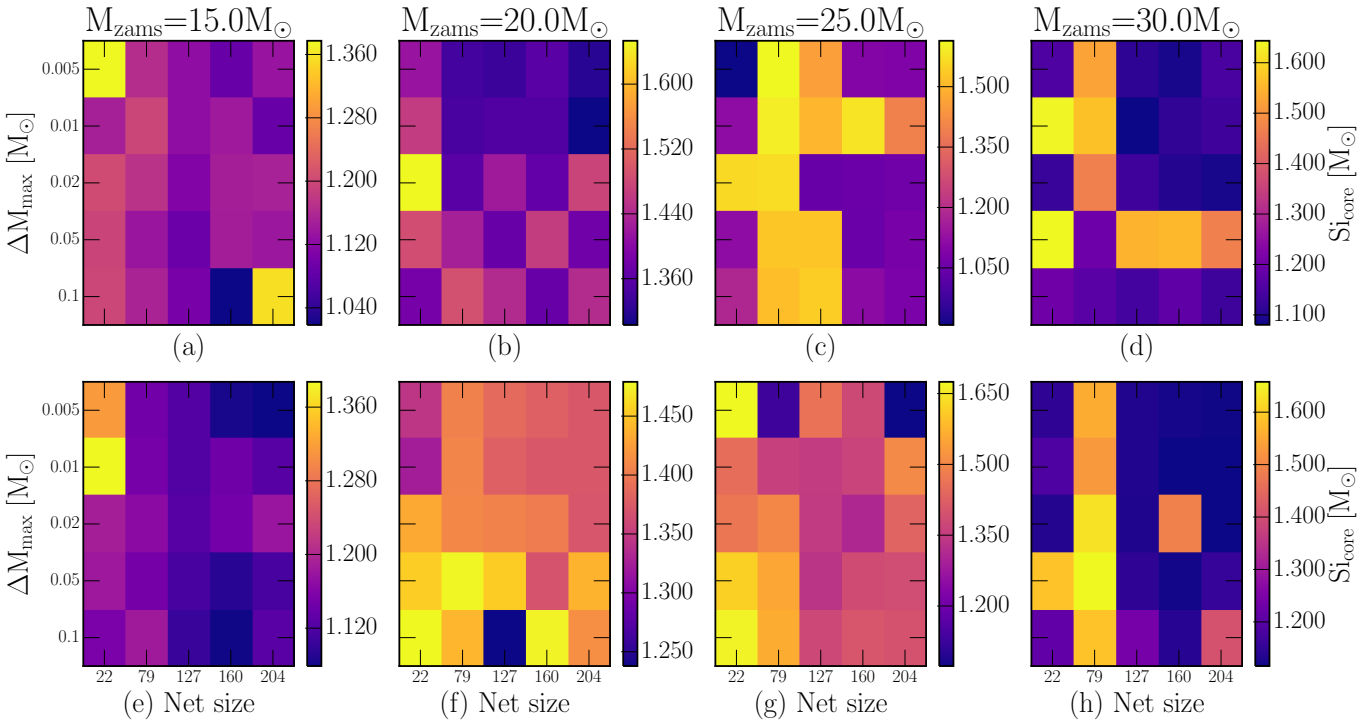

Figure 17. Silicon core mass at silicon ignition, defined when $\log_{10}(T_c/K) = 9.5$, as a function of the number of isotopes in the reaction network and mass resolution. Top: for `MESA` models without mass loss. Bottom: with mass loss.

topes in the reaction network. For a fixed ΔM_{max}, in most cases, the final Fe-core mass for models using the `mesa_127.net`, `mesa_160.net`, and `mesa_204.net` reaction networks agree to within $\approx 0.05\,M_\odot$. In some cases, the `approx22.net` and `mesa_79.net` reaction networks models produce a more massive Fe-core (≈ 0.07–$0.13\,M_\odot$). This is most noticeable for the $15\,M_\odot$ models without mass loss, where `mesa_160.net` and `mesa_204.net` models yield an Fe core of $\approx 1.33\,M_\odot$ while the `approx22.net` model gives $M_{Fe} \approx 1.51\,M_\odot$, an $\approx 14\%$ difference.

The definition of the final Fe-core mass is worthy of mention. We use `MESA`'s definition, which is the maximum mass location where $X(^{56}Fe) > 0.1$ and $X(^{28}Si) < 0.01$. Other options for defining the Fe-core mass include the location of the maximum infall velocity, a fixed Y_e value, or the Y_e jump (Woosley & Weaver 1995; Heger et al. 2001). Comparing the different measures, we find the median Fe-core mass using `MESA`'s abundance definition is $\approx 0.01\,M_\odot$ less than that when using the peak velocity location. When using the Y_e jump definition the core mass is $\approx 0.03\,M_\odot$ greater than the peak velocity location. A fixed Y_e definition was found to be unsuitable due to variations between the models in the Y_e value outside the Fe-core, which could lead to changes as large as $\approx 0.5\,M_\odot$ in the core mass location. Consideration needs to be given to finding a consistent and reliable definition for the final core mass, to enable comparisons between different models. We do not claim that `MESA`'s definition is superior.

For a fixed reaction network, say `mesa_160.net`, Figure 20 shows that mass resolution can have a significant impact on the final Fe-core mass. The largest spread occurs for the $M_{ZAMS} = 25\,M_\odot$ where the Fe-core mass ranges from ≈ 1.38 - $1.8\,M_\odot$. For the $25\,M_\odot$ model the core masses split into two groups based on the resolution, a similar trend to that seen in its He-core mass (Figure 6), those models with lower He-core masses have grown smaller iron core masses. However, for mass resolutions of $\Delta M_{max} \leq 0.01$, the final Fe-core mass is monotonic as the ZAMS mass increases, and agrees to within $\pm 0.1\,M_\odot$ as the resolution increases. Whether the monotonic trend at the highest mass resolutions remains monotonic with a significantly finer grid of ZAMS masses is under consideration (I. Petermann et al, in prep).

In comparing the mass loss models against those without, we find the iron core masses are slightly smaller on average with mass loss. However the decrease in the mass of the cores is much less than the decrease in the final mass. For instance the $30\,M_\odot$ models may lose $\approx 10\,M_\odot$ of material over their lifetime (Table 1), yet the iron cores will only be ≈ 0.1–$0.2\,M_\odot$ smaller. Mass loss rates are uncertain for the mass range considered here, but we have show that the size of the iron cores are only mildly sensitive to the total amount of mass lost.

Figure 20 shows that the choice of reaction network

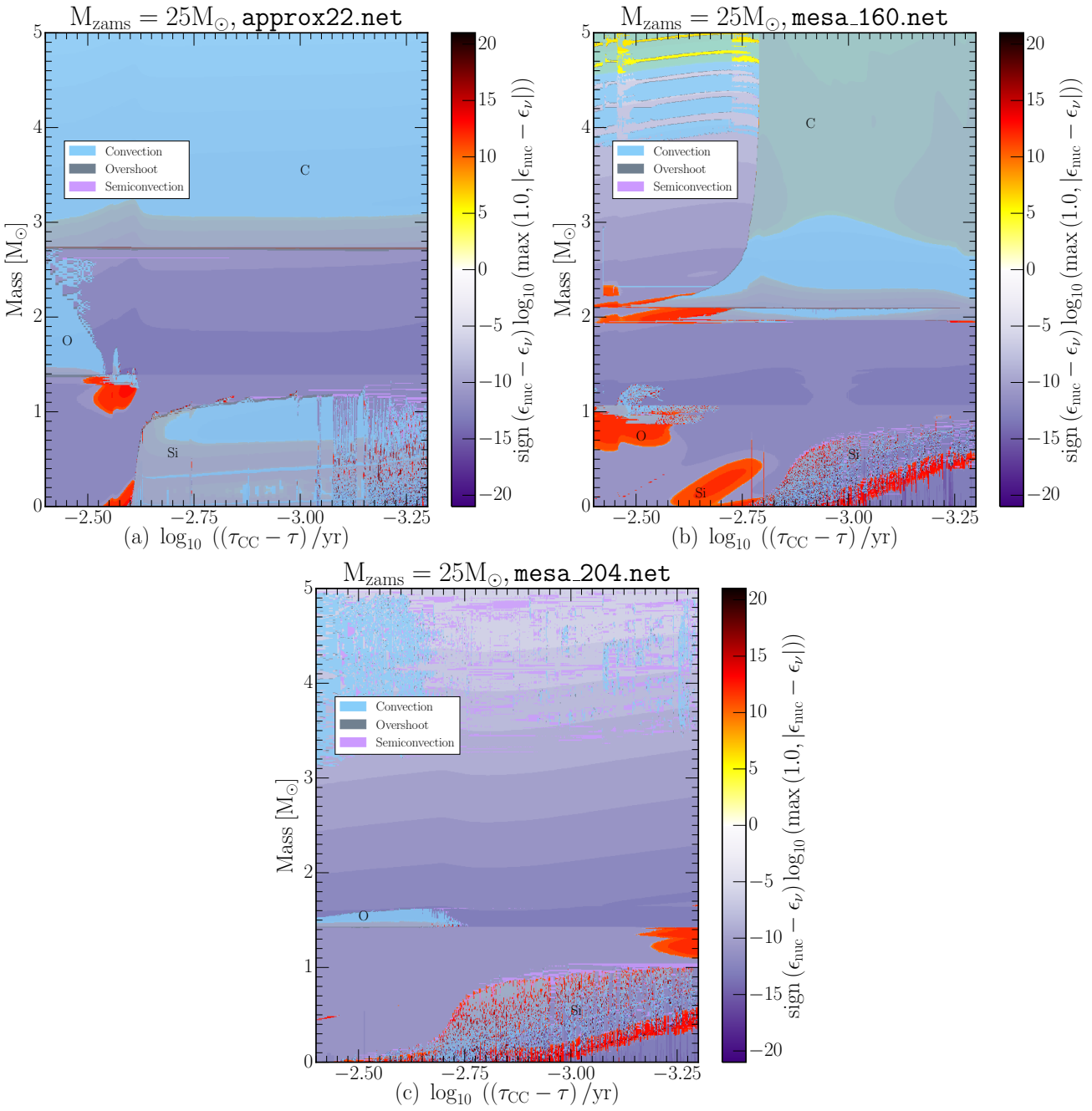

Figure 18. Core Si-burning Kippenhan plots of the $M_{ZAMS} = 25\,M_\odot$ models with mass loss and $\Delta M_{max} = 0.005\,M_\odot$ for various reaction networks. Top left (a), `approx22.net`; Top right (b), `mesa_160.net`; Bottom (c), `mesa_204.net`. Time is measured in years until core-collapse. Fuels driving selected radiative or convective regions are labeled.

can directly affect the final value of M_{Fe}. In turn, this determines the location of the maximum infall velocity. This is most notable in Figure 21 for the $M_{ZAMS} = 15\,M_\odot$ models, where the infall velocity occurs ≈ 1.51 $M_\odot$ and 1.55 $M_\odot$ for the `approx22.net` and `mesa_79.net`, respectively. For the larger networks, the core infall velocity occurs at arithmetic mean mass location of $1.4^{+0.02}_{-0.04}$ $M_\odot$. The 20–30 $M_\odot$ stars in Figure 21 follow similar trends, with `approx22.net` and `mesa_79.net` producing the largest deviations about the arithmetic mean Fe core value of $\approx$ 0.07-0.13 $M_\odot$. The 15 $M_\odot$ models, with $\Delta M_{max} = 0.005$, mass loss, and either the `mesa_127.net` or `mesa_160.net` have anomalously low $M_{Fe} < 1.0\,M_\odot$, these models achieve our definition of core collapse infall velocity in a few spatial zones but they are not undergoing a collapse and thus the evolution terminates early before the core could grow to its full extent.

Figure 21 shows the Y_e and radial velocity profiles at core-collapse for the M_{ZAMS}=15, 20, 25, and 30 $M_\odot$

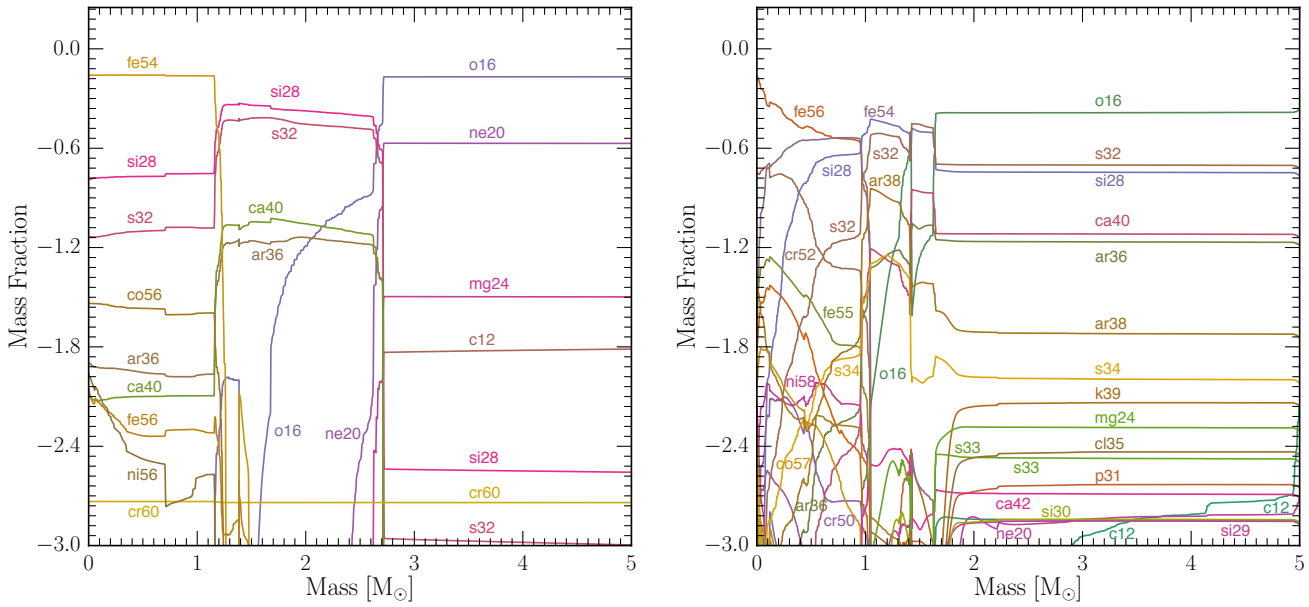

Figure 19. Mass Fraction profiles for the two $M_{ZAMS} = 25\,M_\odot$ models shown in Figure 18 at $\log_{10}((\tau_{cc} - \tau)/\mathrm{yr}) = -3.0$ for (left panel) the `approx22.net` reaction network and (right panel) the `mesa_204.net` reaction network.

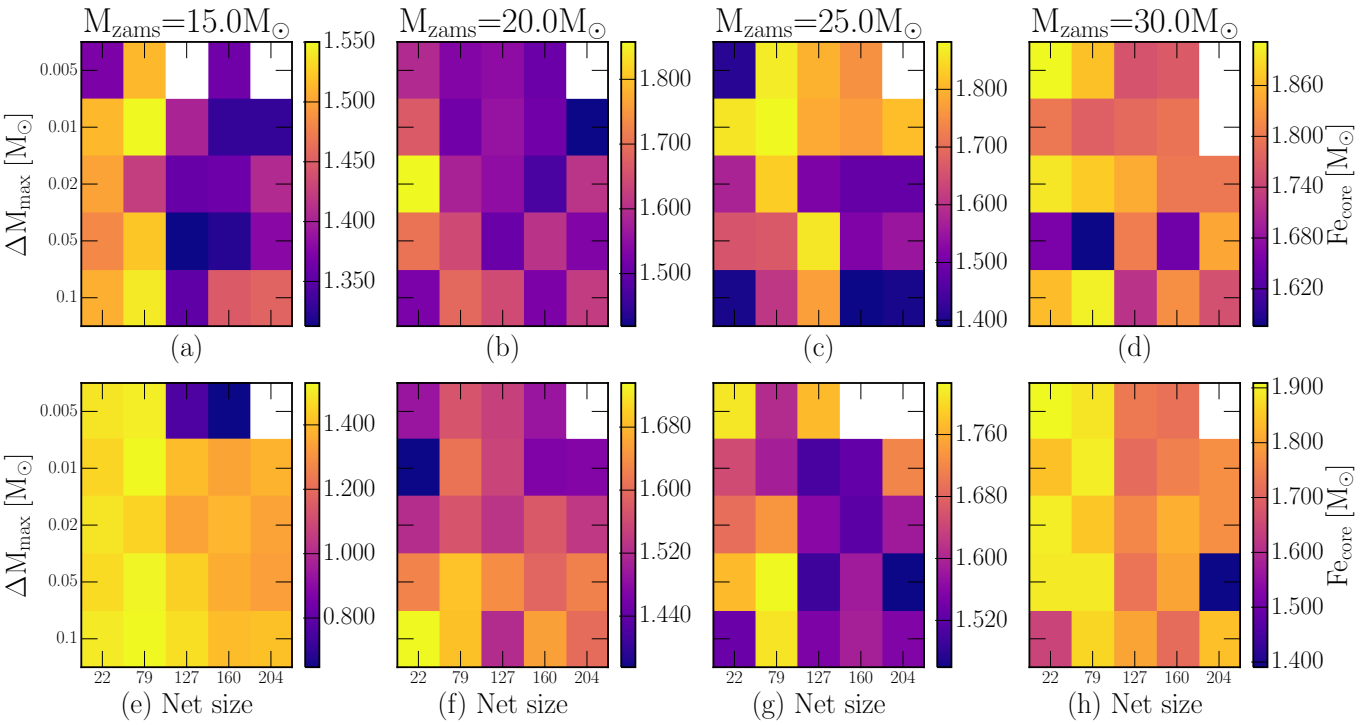

Figure 20. Iron core mass at core-collapse, defined when $v > 1000$ km s^{-1}, as a function of the number of isotopes in the reaction network and mass resolution. Top row: for `MESA` models without mass loss. Bottom row: for models with mass loss. White squares denote models that did not reach core-collapse.

models with mass loss and $\Delta M_{max} = 0.01\,M_\odot$ for different reaction networks. In most cases, we find that the models with the `approx22.net` reaction network under-estimates the $Y_{e,c}$ when compared to the larger reaction networks. The converse is found for models using the `mesa_79.net` network which tends to over-estimate $Y_{e,c}$. For example, in the $M_{ZAMS} = 15\,M_\odot$ case, the models using the `mesa_127.net`, `mesa_160.net`, and `mesa_204.net` reaction networks converge to $Y_{e,c} \approx 0.43$. However, models using the smaller `approx22.net` and `mesa_79.net` reaction networks give values of $Y_e \approx 0.41$ and $Y_e \approx 0.46$, respectively. A similar trend is found

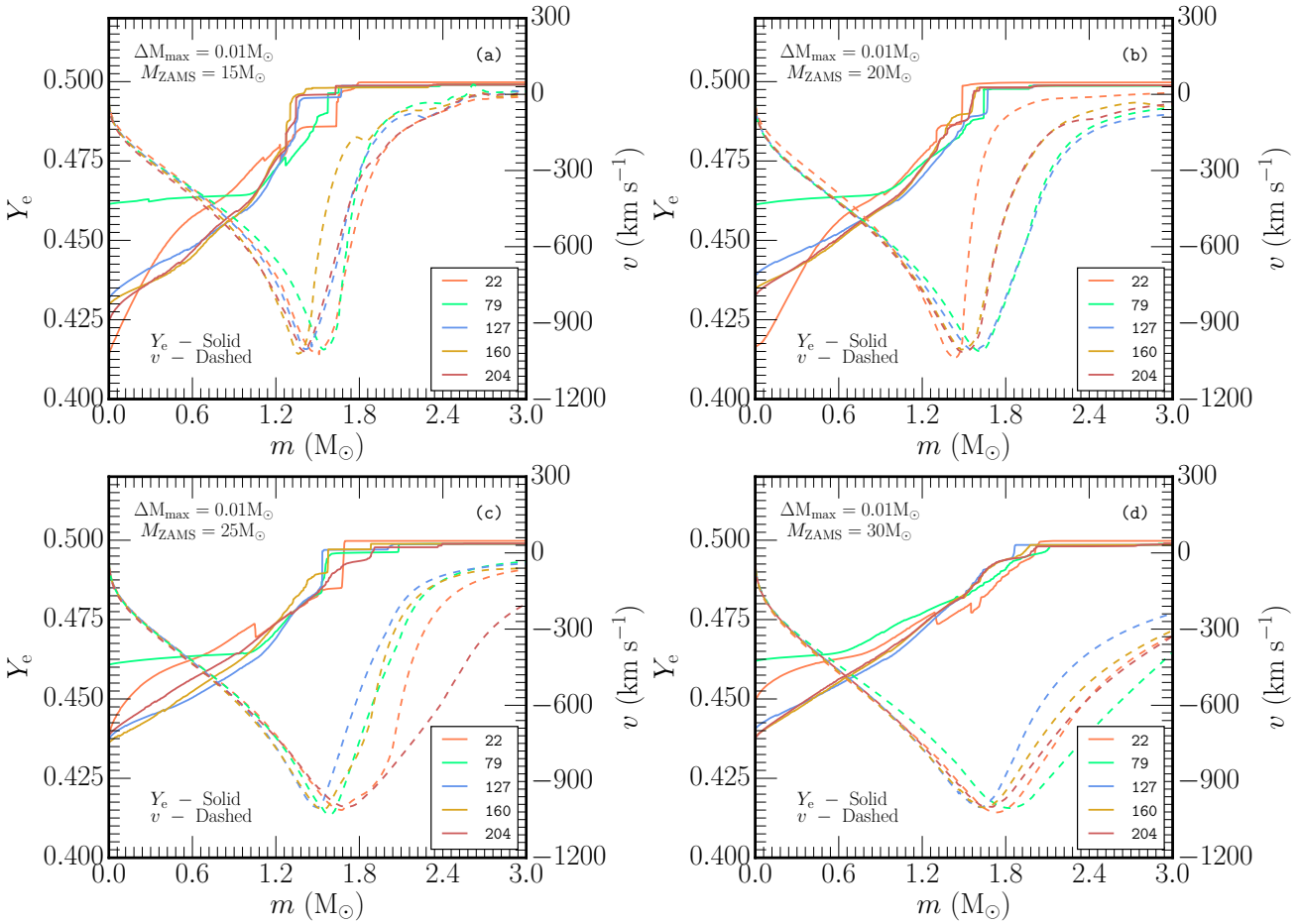

Figure 21. The electron fraction Y_e (solid curves) and radial velocity (dashed curves) at core-collapse for $M_{ZAMS} = 15$, 20, 25, and 30 $M_\odot$ models with mass loss and $\Delta M_{max} = 0.01\,M_\odot$ Color denotes the number of isotopes used in the reaction network.

for the $M_{ZAMS} = 20\,M_\odot$ models. In the case of the $M_{ZAMS} = 25$ and $30\,M_\odot$ models, the `approx22.net` and `mesa_79.net` reaction networks show less disagreement in $Y_{e,c}$ with the values found for the larger networks. The final $Y_{e,c}$ is set by the final composition of the core, in the `approx22.net` this is a mixture of ^{56}Fe and ^{60}Cr, the `mesa_79.net` are $\approx 95\%$ ^{56}Fe (independent of mass), while in the larger networks the core becomes a mixture of iron groups elements. This is due to the `mesa_79.net` missing ^{55}Fe, $^{48-51}$V and $^{51-56}$Cr isotopes, which are present in the larger nuclear networks. These additional isotopes provide alternate decay routes for the ^{56}Fe in the core.

There is also considerable variation in the shape of the Y_e step at the edge of the iron core. This is not a well defined jump in the Y_e value but can show a number of sub steps. For instance, for the $15\,M_\odot$ models in Figure 21 the `approx22.net` has a single large jump at $1.62\,M_\odot$ while with the larger nets the jump is at $1.3\,M_\odot$ but shows substructure in the Y_e values.

Figure 22 shows the oxygen mass fraction profile at core-collapse for a subset of the $M_{ZAMS} = 20\,M_\odot$ models. For each profile, all isotopes of oxygen in a particular network are summed to give the total oxygen mass fraction as a function of mass coordinate (see Figure 1 for the different isotopes of oxygen included for each network). The left panel plots the $X(O)$ profile as a function of the number of isotopes in the network for the $M_{ZAMS} = 20\,M_\odot$ models without mass loss at a mass resolution of $\Delta M_{max} = 0.01\,M_\odot$. The right panel plots the $X(O)$ profile as a function of mass resolution for the $M_{ZAMS} = 20\,M_\odot$ models without mass loss that use the `mesa_160.net` reaction network (this network follows $^{14-18}$O).

The upper mass boundary of the O shell is well constrained at $4.4\,M_\odot$ for the different networks at a fixed $\Delta M_{max} = 0.01\,M_\odot$ models. While the lower mass boundary varies over $0.5\,M_\odot$, the total mass of oxygen only varies between $1.9 - 2.0\,M_\odot$. For the models with a fixed reaction network and variable ΔM_{max} the upper mass boundary varies over $\approx 0.2\,M_\odot$, similar to the spread in the lower mass boundary. Most models show a top hat shape due to strong convection occurring over the shell, while the $\Delta M_{max} = 0.1\,M_\odot$, `mesa_160.net` shows a different behavior due to an oxygen burning wave propagating from the base of the O shell outwards.

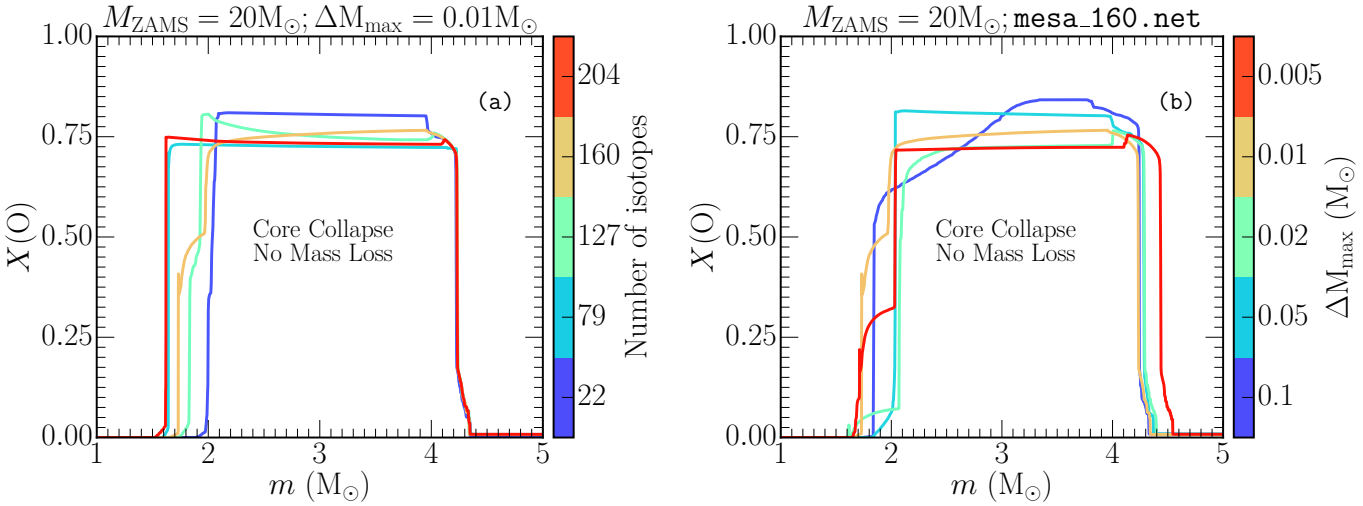

Figure 22. O mass fraction profile at core-collapse for the $M_{\rm ZAMS} = 20\,M_\odot$ model without mass loss as a function of `(a)` the number of isotopes in the nuclear reaction network and `(b)` the mass resolution $\Delta M_{\rm max}$.

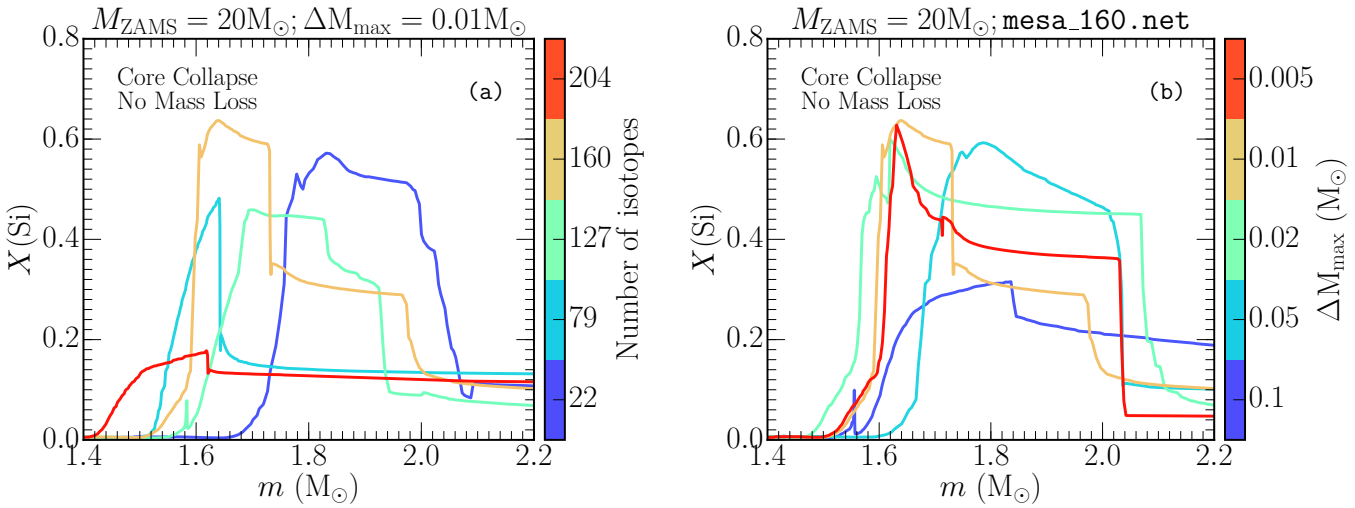

Figure 23. Si mass fraction profile at core collapse for the $M_{\rm ZAMS} = 20\,M_\odot$ model without mass loss as a function of `(a)` the number of isotopes in the nuclear reaction network and `(b)` the mass resolution $\Delta M_{\rm max}$.

The almost step like feature seen in the lower boundaries is due to a convective Si-burning shell, abutting into the base of O-burning shell and the top of the Fe-core. This Si-burning shell only partially burns the silicon and the oxygen before core-collapse.

Similarly, in Figure 23 we show mass fraction profiles for X(Si) for $M_{\rm ZAMS} = 20\,M_\odot$ models without mass loss. This region shows considerably more variation than the O shells in Figure 22. The lower mass boundary of the silicon distribution denotes the edge of the iron core, while the upper mass boundary denotes the edge between the Si shell and the base of the O shell.

For fixed mass resolution of $\Delta M_{\rm max} = 0.01\,M_\odot$ there are three groupings in the left panel of Figure 23; the `approx22.net`; the `mesa_79.net`, `mesa_127.net` and `mesa_160.net`; and the `mesa_204.net`. The `approx22.net` model has the largest iron core due to the most energetic shell Si-burning. This pushes the silicon shell outwards and allows the shell to burn over a larger oxygen-rich region. The larger networks are generally cooler in temperature so the Si-burning shell does not extend as far outwards. The sudden drop in the silicon mass fraction, at the upper boundary, seen in the `mesa_79.net`, `mesa_127.net` and `mesa_160.net` models is due to the lower mass boundary of the O shell being convective which mixes silicon outwards. The `mesa_204.net` shows a case when the iron core abuts the O shell, leaving no distinct Si shell.

For a fixed `mesa_160.net` reaction network, Figure 23 shows a trend for the Si shell to move inwards and concentrate at lower mass coordinates as the resolution increases. This is due to the temperature and density of the Si shell decreasing as the resolution increases. This slows the conversion of silicon into iron-group elements.

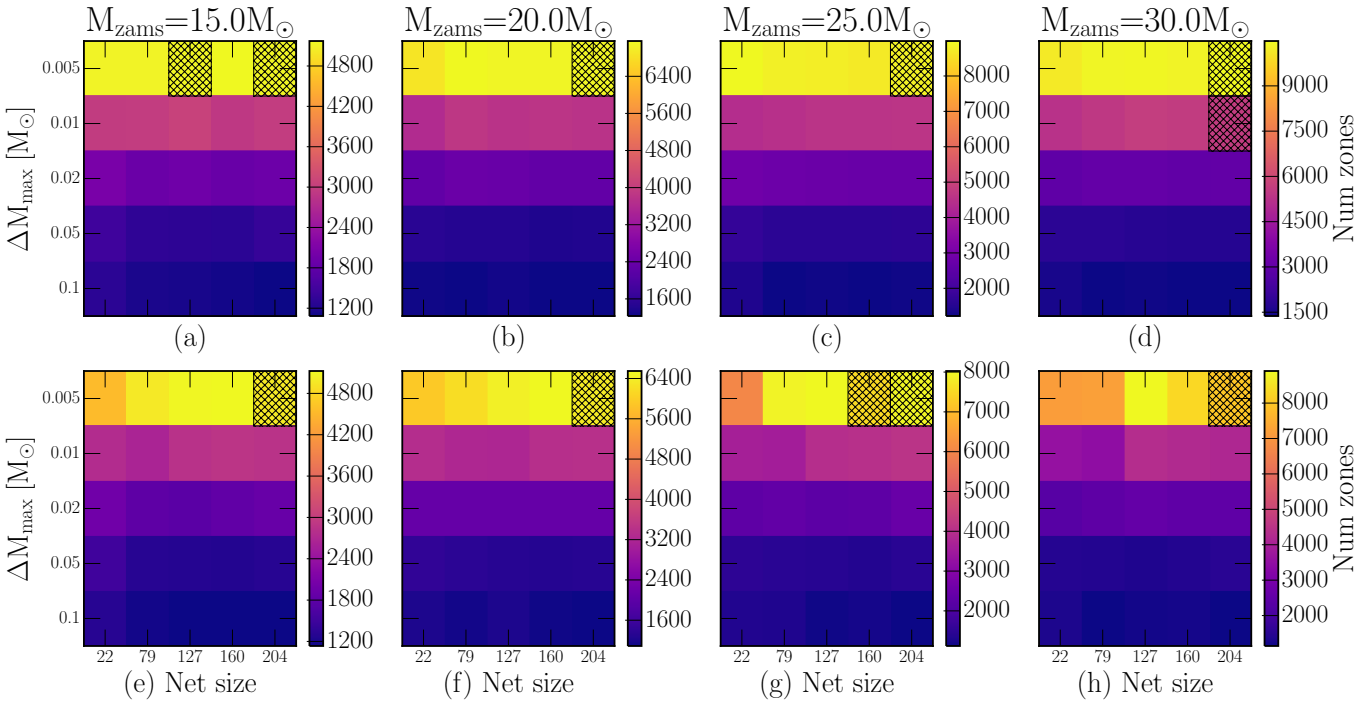

Figure 24. Total number of spatial zones at core-collapse as a function of the number of isotopes in the network and mass resolution. Top: for `MESA` models without mass loss. Bottom: with mass loss. Hatching indicates models that did not reach core-collapse.

For models with $\Delta M_{max} \leq 0.02\,M_\odot$ the lower mass boundary of the silicon is sharply defined at $\approx 1.6\,M_\odot$, with the core being composed primarily of ^{54}Fe up to the edge of the iron core. For the $\Delta M_{max} = 0.1\,M_\odot$ and $\Delta M_{max} = 0.5\,M_\odot$ models the lower mass boundary is more inclined due to the increased presence of ^{56}Ni. In the $\Delta M_{max} = 0.1\,M_\odot$ case, this becomes a distinct ^{56}Ni shell between the iron core, which is mostly ^{54}Fe, and the silicon shell. In the $\Delta M_{max} = 0.05\,M_\odot$ case ^{54}Fe and ^{56}Ni are approximately equal components at $\approx 25\%$ at the interface of the ^{54}Fe core and the Si shell.

Figure 24 shows the total number of mass zones at core-collapse. As ΔM_{max} increases from $\Delta M_{max} = 0.1\,M_\odot$ to $0.005\,M_\odot$ there is a factor four increase in the number of zones, which is much less than the factor 20 increase in ΔM_{max}. This is due to ΔM_{max} only providing an upper limit on the mass of a cell. For instance, a $M_{ZAMS} = 15\,M_\odot$ model with $\Delta M_{max} = 0.1\,M_\odot$, assuming all cells have the same ΔM_{max}, needs only 150 spatial zones – much less than the 1200 zones present in our models. On average we find that the models with mass loss need slightly less zones at core collapse. This is due to having a smaller mass star. However, due to the fact that the zones are unevenly distributed, being concentrated near the core and where large changes in stellar properties occur, the scaling is not linear with the star's mass. There are a number of other `MESA` controls that effect the spatial resolution, like δ_{mesh}, which contribute to the total number of zones, and their relative distribution. We recommend taking a critical view of the spatial distribution of zones in stellar models and consider the effect of increased resolution on their results.

Table 1 summarizes the pre-SN model properties measured either during the evolution of the model or at core collapse. We show the median value over all models with upper and lower bounds. The $He_{core}, C_{core}, O_{core}, Si_{core}$ summarize the core masses at the point of the fuel ignition (See Figures 6, 9, 14, 17, for a illustration of their spread). Similarly the $Y_{e,c}$ shows the electron fraction at the center of the star measured at the same time as the core masses. The electron fraction does not drop much bellow 0.5 until after oxygen burning. Once silicon burning commences the $Y_{e,c}$ drops to 0.48–0.49, with larger initial mass stars having larger $Y_{e,c}$. At core collapse $Y_{e,c}$ can drop to $Y_{e,c} = 0.43$–0.44, with larger initial masses having larger median values, however the upper/lower bounds overlap between all the masses.

Table 1 lists the final masses (M_{final}) at core-collapse, but dominated by the mass at the TAMS, for models with mass loss. Similarly to final ages, most of the variation in the final masses occurs as mass resolution increases (see Section 3.2). For the $M_{ZAMS} = 15\,M_\odot$ models the total variation in the final mass is $\simeq 2\%$. As the ZAMS mass increases, this variation increases to $\simeq 10\%$ for the $M_{ZAMS} = 30\,M_\odot$ models. In general, as the resolution increases the final mass decreases, consistent with the findings from Section 3.1, where the higher resolu-

tion models live longer due to the change in behavior of the ICZ and SCZ.

Table 1. Median pre-SN model properties, with upper and lower bounds

Property	$15\,M_\odot$		$20\,M_\odot$		$25\,M_\odot$		$30\,M_\odot$	
	$\dot{M}=0$	$\dot{M}\neq 0$	$\dot{M}=0$	$\dot{M}\neq 0$	$\dot{M}=0$	$\dot{M}\neq 0$	$\dot{M}=0$	$\dot{M}\neq 0$
He_{core} $[M_\odot]^{a,b}$	$2.82^{2.82}_{2.79}$	$2.77^{2.78}_{2.72}$	$4.67^{4.70}_{4.59}$	$4.57^{4.59}_{4.52}$	$6.88^{7.28}_{6.80}$	$6.56^{6.67}_{6.52}$	$9.44^{9.89}_{9.15}$	$8.67^{8.78}_{8.62}$
C_{core} $[M_\odot]$	$2.51^{2.58}_{2.49}$	$2.44^{2.53}_{2.43}$	$4.19^{4.75}_{4.04}$	$4.07^{4.08}_{3.69}$	$6.02^{6.43}_{4.34}$	$5.75^{5.92}_{5.53}$	$8.28^{8.79}_{7.13}$	$7.62^{7.82}_{7.22}$
O_{core} $[M_\odot]$	$1.41^{1.43}_{1.35}$	$1.40^{1.42}_{1.32}$	$1.54^{2.47}_{1.43}$	$1.57^{2.05}_{1.41}$	$2.34^{3.04}_{1.74}$	$1.81^{2.47}_{1.76}$	$2.38^{3.18}_{2.14}$	$2.39^{3.06}_{2.26}$
Si_{core} $[M_\odot]$	$1.15^{1.38}_{1.02}$	$1.15^{1.39}_{1.08}$	$1.38^{1.65}_{1.30}$	$1.40^{1.48}_{1.24}$	$1.19^{1.61}_{0.91}$	$1.40^{1.67}_{1.07}$	$1.16^{1.64}_{1.08}$	$1.15^{1.66}_{1.12}$
$Ye_{c,He}$ [b]	$0.505^{0.505}_{0.505}$	$0.505^{0.505}_{0.505}$	$0.505^{0.505}_{0.505}$	$0.505^{0.505}_{0.505}$	$0.505^{0.505}_{0.505}$	$0.505^{0.505}_{0.505}$	$0.505^{0.505}_{0.505}$	$0.505^{0.505}_{0.505}$
$Ye_{c,C}$	$0.499^{0.500}_{0.499}$	$0.499^{0.500}_{0.499}$	$0.499^{0.500}_{0.499}$	$0.499^{0.500}_{0.499}$	$0.499^{0.500}_{0.499}$	$0.499^{0.500}_{0.499}$	$0.499^{0.500}_{0.499}$	$0.499^{0.500}_{0.499}$
$Ye_{c,O}$	$0.499^{0.500}_{0.498}$	$0.499^{0.500}_{0.498}$	$0.499^{0.500}_{0.498}$	$0.499^{0.500}_{0.498}$	$0.498^{0.500}_{0.498}$	$0.499^{0.500}_{0.484}$	$0.498^{0.500}_{0.498}$	$0.498^{0.500}_{0.490}$
$Ye_{c,Si}$	$0.486^{0.498}_{0.475}$	$0.486^{0.498}_{0.475}$	$0.488^{0.498}_{0.483}$	$0.489^{0.498}_{0.483}$	$0.491^{0.497}_{0.483}$	$0.490^{0.499}_{0.482}$	$0.491^{0.498}_{0.489}$	$0.490^{0.497}_{0.488}$
$Ye_{c,Fe}$	$0.431^{0.461}_{0.419}$	$0.432^{0.461}_{0.414}$	$0.438^{0.462}_{0.425}$	$0.438^{0.462}_{0.416}$	$0.438^{0.462}_{0.414}$	$0.438^{0.462}_{0.423}$	$0.444^{0.462}_{0.437}$	$0.442^{0.462}_{0.428}$
τ_H [Myr][c]	$10.95^{10.96}_{10.93}$	$10.99^{11.00}_{10.94}$	$7.73^{7.74}_{7.72}$	$7.78^{7.79}_{7.76}$	$6.18^{6.51}_{6.16}$	$6.24^{6.38}_{6.22}$	$5.53^{5.62}_{5.26}$	$5.34^{5.43}_{5.33}$
τ_{He} [Myr]	$1.69^{1.71}_{1.48}$	$1.74^{1.75}_{1.51}$	$1.11^{1.72}_{1.05}$	$1.10^{1.29}_{1.08}$	$0.81^{1.19}_{0.77}$	$0.82^{0.89}_{0.81}$	$0.65^{0.73}_{0.63}$	$0.69^{0.74}_{0.68}$
τ_C [yr]	$78.37^{82.62}_{75.65}$	$81.80^{87.04}_{76.15}$	$111.36^{115.61}_{25.90}$	$125.42^{131.19}_{28.52}$	$27.06^{28.42}_{14.81}$	$23.35^{26.98}_{22.53}$	$16.56^{22.45}_{7.97}$	$19.82^{22.62}_{15.11}$
τ_O [yr]	$3.83^{5.05}_{3.28}$	$4.08^{5.36}_{3.51}$	$1.44^{2.76}_{0.16}$	$1.28^{3.12}_{0.26}$	$0.14^{0.29}_{0.08}$	$0.31^{0.93}_{0.01}$	$0.13^{0.19}_{0.02}$	$0.14^{0.16}_{0.10}$
τ_{Si} [days]	$3.43^{5.05}_{0.74}$	$3.74^{5.60}_{0.75}$	$0.81^{1.56}_{0.32}$	$0.91^{2.04}_{0.27}$	$0.61^{6.58}_{0.18}$	$0.66^{1.59}_{0.16}$	$0.35^{1.92}_{0.15}$	$0.41^{1.97}_{0.21}$
τ_{Fe} [hr]	$33.16^{57.11}_{11.21}$	$36.38^{74.01}_{11.87}$	$11.11^{35.22}_{3.66}$	$11.63^{17.95}_{6.59}$	$6.57^{25.25}_{4.04}$	$9.55^{19.72}_{4.26}$	$4.74^{24.33}_{3.23}$	$4.77^{25.36}_{3.37}$
He_{shell} $[M_\odot]^{d,e}$	$4.17^{4.22}_{4.16}$	$4.09^{4.17}_{4.08}$	$6.20^{6.88}_{6.09}$	$6.05^{6.07}_{5.84}$	$8.26^{8.71}_{8.12}$	$7.95^{8.10}_{7.71}$	$10.87^{11.30}_{9.66}$	$9.99^{10.24}_{9.58}$
C_{shell} $[M_\odot]$	$2.51^{2.58}_{2.49}$	$2.44^{2.54}_{2.43}$	$4.19^{4.75}_{4.04}$	$4.07^{4.09}_{3.61}$	$6.03^{6.44}_{5.84}$	$5.76^{5.88}_{5.54}$	$8.26^{8.73}_{7.09}$	$7.57^{7.82}_{7.16}$
O_{shell} $[M_\odot]$	$2.42^{2.53}_{2.18}$	$2.33^{2.49}_{2.13}$	$3.95^{4.14}_{3.27}$	$3.82^{3.93}_{2.61}$	$5.38^{5.69}_{4.08}$	$5.25^{5.63}_{2.80}$	$6.87^{8.20}_{5.64}$	$6.47^{7.20}_{4.68}$
Si_{shell} $[M_\odot]$	$1.59^{1.70}_{0.00}$	$1.61^{1.65}_{1.24}$	$1.80^{2.97}_{1.56}$	$1.81^{2.11}_{0.00}$	$1.90^{2.67}_{1.53}$	$1.88^{2.22}_{1.62}$	$2.27^{2.58}_{1.73}$	$2.30^{3.14}_{1.50}$
Fe_{core} $[M_\odot]$	$1.41^{1.55}_{0.75}$	$1.42^{1.53}_{0.77}$	$1.55^{1.86}_{1.35}$	$1.57^{1.74}_{1.38}$	$1.66^{1.88}_{1.35}$	$1.59^{1.83}_{1.46}$	$1.80^{1.90}_{1.58}$	$1.79^{1.90}_{1.39}$
H_{env} $[M_\odot]^{d,f}$	$6.96^{7.21}_{6.94}$	$5.65^{6.14}_{5.59}$	$8.41^{8.55}_{7.58}$	$6.74^{7.18}_{6.50}$	$9.76^{9.96}_{9.17}$	$6.09^{7.22}_{4.69}$	$10.47^{11.02}_{9.99}$	$4.60^{6.10}_{0.00}$
M_{final} $[M_\odot]^{d,g}$	...	$13.02^{13.37}_{12.94}$	...	$17.26^{18.11}_{16.91}$	...	$18.95^{21.17}_{17.01}$	...	$20.27^{22.06}_{17.38}$
$\log_{10}$ $(R/R_\odot)^d$	$2.97^{2.99}_{2.96}$	$2.98^{3.00}_{2.97}$	$3.08^{3.08}_{3.06}$	$3.07^{3.07}_{3.05}$	$3.08^{3.09}_{3.05}$	$3.07^{3.08}_{3.05}$	$2.97^{3.02}_{2.92}$	$2.99^{3.03}_{2.95}$
$\log_{10}$ $(T_{eff}/K)^d$	$3.50^{3.51}_{3.50}$	$3.50^{3.52}_{3.49}$	$3.52^{3.53}_{3.51}$	$3.52^{3.53}_{3.51}$	$3.56^{3.58}_{3.55}$	$3.56^{3.73}_{3.54}$	$3.65^{3.74}_{3.62}$	$3.63^{3.67}_{3.60}$
$\log_{10}$ $(L/L_\odot)^d$	$4.91^{4.93}_{4.90}$	$4.90^{5.01}_{4.88}$	$5.18^{5.23}_{5.13}$	$5.15^{5.20}_{5.09}$	$5.36^{5.42}_{5.30}$	$5.33^{6.03}_{5.25}$	$5.47^{5.84}_{5.38}$	$5.49^{5.56}_{5.40}$
$\xi_{M=2.5}$ [d,h]	$0.10^{0.15}_{0.04}$	$0.08^{0.13}_{0.04}$	$0.24^{0.63}_{0.10}$	$0.24^{0.43}_{0.13}$	$0.32^{0.66}_{0.16}$	$0.27^{0.60}_{0.19}$	$0.60^{0.69}_{0.31}$	$0.58^{0.69}_{0.19}$

[a] Core mass values, see Figures 6, 9, 14, 17, 20 for definitions.

[b] Measured at the corresponding ignition of each fuel, except for Fe which is measured at core collapse.

[c] Approximate time to transition to the next major fuel source.

[d] Measured at core collapse.

[e] Outer mass coordinate where the element is the most abundant.

[f] Mass of H-rich envelope.

[g] Total mass of star.

[h] Compactness parameter, with $M = 2.5\,M_\odot$.

The τ values in Table 1 denote the time between the depletion of the previous fuel to the core ignition of the next. As we progress between each major fuel source the lifetime of the star decreases rapidly, as expected. As the initial mass increases the lifetime for each fuel to burn decreases, and the fraction of the stars life spent

burning each fuel (other than hydrogen) decreases. For instance the MS lifetime of a $15\,M_\odot$ star is twice that of the $30\,M_\odot$ but eight times that during the final silicon shell burning. Also those stars that lose mass, live longer than their non mass losing companions due to the slower evolution experienced by a lower mass star. $He_{shell}, C_{shell}, O_{shell}, Si_{shell}$ denote the locations of each fuel shell at core collapse, while the Fe_{core} is the iron core mass at core collapse (see Figure 20). The shell locations increase as the initial mass increases, with mass losing stars having smaller shell masses. The Si_{shell} lower bound of 0.0 does not denote that there is a distribution to 0.0, but that a few models have no silicon shell (see Figure 23) while the other models sit near the median value.

Lastly we provide a summary of the surface of the star at core collapse. H_{env} is the mass of H-rich envelope, M_{final} is the final mass and $R/R_\odot, T_{eff}, L/L_\odot$ provide the surface radius, temperature and luminosity. As the initial mass increases the temperature and luminosity of the models increase, but the surface radius is maximum for the 20–25 $M_\odot$ models before decreasing for the $30\,M_\odot$ models. Mass loss also does not significantly effect the final radius, temperature or luminosity even though they can be significantly smaller and have much smaller H_{env} values. The final compactness parameter, is given by,

$$\xi = \frac{(M/\,M_\odot)}{R_{M=2.5}/1000\text{km}} \tag{5}$$

where $M = 2.5\,M_\odot$ and the radius is measured (in km) at the radius where $M = 2.5\,M_\odot$ (O'Connor & Ott 2011). In principle it should be measured at the bounce, however Sukhbold & Woosley (2014) showed that no substantial accuracy is lost if measured in the pre-SN model. We see a steady increase in the final value as the initial mass increases, with mass losing stars having slightly smaller values. All the parameters in Table 1 show considerable spread in their values due to changes in the spatial resolution and choice of nuclear network.

3.9. *Pre-SN Nucleosynthesis*

Figure 25 shows the stable isotopes from hydrogen to zinc for the pre-SN $M_{ZAMS} = 15$, 20, 25, and $30\,M_\odot$ models with mass loss, $\Delta M_{max} = 0.01\,M_\odot$, and the `mesa_204.net` reaction network. These pre-SN yields are for the stable isotopes outside the Fe-core. The x-axis is the atomic mass number. The y-axis is the logarithmic ratio of the model mass fraction to the Grevesse & Sauval (1998) solar mass fraction. The most abundant isotope of a given element is marked by an asterisk and isotopes of the same element are connected by solid lines.

Isotopes in Figure 25 heavier that about calcium will be strongly impacted by the explosion. Up to calcium, however, it generally makes little difference whether the pre-SN or the exploded yields are used (e.g., Timmes et al. 1995). In a forthcoming effort we anticipate exploding the pre-SN models examined in this paper. With this limitation of interpreting pre-SN yields in mind, the overall average production factor of ≈ 20 for the $M_{ZAMS} = 15\,M_\odot$ model and rising to ≈ 100 for the $M_{ZAMS} = 30\,M_\odot$ model are commensurate with existing pre-SN yields (e.g., Woosley & Weaver 1995; Limongi & Chieffi 2003; Chieffi & Limongi 2013) and the production factors needed by galactic chemical evolution models (e.g., Gibson et al. 2003) to reproduce the solar composition. Part of the spread below calcium is a consequence of uncertain physics in the `MESA` models: the treatment of convective, semiconvective, and overshoot mixing, the parameterization of mass loss, nuclear reaction rates, and residual uncertainty in the measured solar abundances. Post-SN the yields for isotopes with $A > 40$ will also depend sensitively on choice of explosion dynamics (Paxton et al. 2015).

The light isotopes ^{6,7}Li, ^{9}Be, and ^{10,11}B are not plotted in Figure 25 as the primary source of these isotopes is commonly taken to be big-bang nucleosynthesis (e.g., Coc et al. 2012; Cyburt et al. 2016), spallation of CNO nuclei in the interstellar medium by cosmic rays (e.g., Reeves et al. 1970; Olive & Schramm 1992; Ramaty et al. 2000; Fields et al. 2000; Prantzos 2012) or the ν-process during the explosion (e.g., Woosley et al. 1990; Balasi et al. 2015).

The isotopes ^{12,13}C and ^{14}N are under produced in Figure 25 by ≈ 3 relative to the average overproduction factor for the $M_{ZAMS} = 15\,M_\odot$ model and by ≈ 20 relative to the average overproduction factor for the $M_{ZAMS} = 30\,M_\odot$ model. This is consistent with the bulk of these isotopes being produced during CNO processing and dredged-up material from helium shell flashes in intermediate and low mass stars (Iben & Truran 1978; Renzini & Voli 1981; Doherty et al. 2014; Karakas & Lugaro 2016).

The solar ^{29}Si abundance is ≈ 1.4 times larger than the solar ^{30}Si abundance, in concordance with observations of some individual stars (Peng et al. 2013) and pre-solar silicon-carbide grains (e.g., Hoppe et al. 2010), yet in tension with common models of 1D core-collapse supernova, Type Ia supernovae, and AGB stars (e.g., Timmes & Clayton 1996; Lugaro et al. 1999; Lewis et al. 2013; Wasserburg et al. 2015). It is curious that the ^{30}Si abundance, normalized to solar in in Figure 25, is larger than the ^{29}Si abundance in the $M_{ZAMS} = 20$ and $30\,M_\odot$ models but traditionally smaller in the $M_{ZAMS} = 15$ and $25\,M_\odot$ models.

The isotope ^{40}K has the largest production factor in the $M_{ZAMS} = 25$ and $30\,M_\odot$ models of Figure 25. This isotope is also a special case as it is radioactive, but the

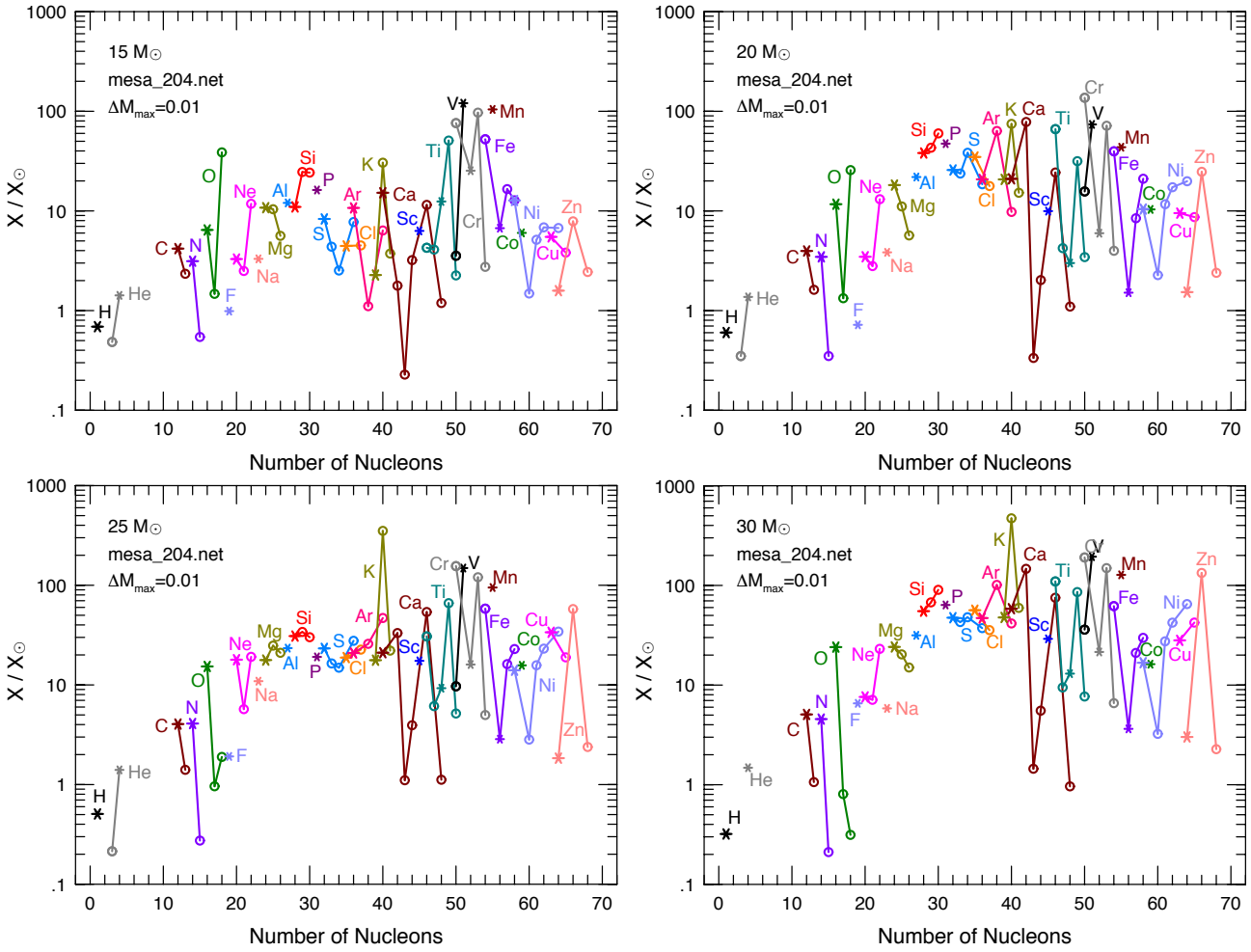

Figure 25. Stable isotopes from hydrogen to zinc for the M_{ZAMS} = 15, 20, 25, and 30 $M_\odot$ models with mass loss, ΔM_{max} = 0.01 $M_\odot$, and the `mesa_204.net` reaction network. The x-axis is the atomic mass number. The y-axis is the logarithmic ratio of the model mass fraction to the Grevesse & Sauval (1998) solar mass fraction. The most abundant isotope of a given element is marked by an asterisk and isotopes of the same element are connected by solid lines.

half-life is long enough (1.248×10^9 yr, Malonda & Carles 2002; Kossert & Günther 2004) that it is included in compilations of the solar composition. The overproduction factor may reflect an uncertain solar abundance.

4. SUMMARY AND DISCUSSION

We have investigated the range of variation in properties of `MESA` pre-SN models with respect to changes in spatial resolution, number of isotopes in the nuclear reaction network, and the inclusion of mass loss. To make this assessment we evolved 200 solar metallicity, non-rotating, single-star models of initial mass M_{ZAMS}=15, 20, 25, and 30 $M_\odot$ from the pre-MS to the onset of core-collapse.

We found that the choice of spatial resolution can have a larger impact on the final states of these models, predominately by altering the state of the star during the MS. This small effect can then be compounded by the relative length of the MS, compared with later evolution stages, to have large impacts on the stellar structure. The choice of nuclear network is also found not to be insignificant even during core helium burning where larger nuclear networks can suppress CBPs. The combination of these effects compounds over the stellar evolution leading to sometimes radically different behaviors between models with the same mass, including differences; in the type of carbon and neon burning, behavior of C, Ne and O shells during silicon burning; and the final mass of the iron core. In the remainder of this section, we discuss our findings and compare them with previous efforts.

Hirschi et al. (2004) considered the pre-SN evolution of non-rotating solar metallicity stellar models with M_{ZAMS} = 12–60 $M_\odot$ from the ZAMS to core Si depletion. We compare the median values of He_{shell} for our mass loss models with M_{ZAMS} =15, 20, and 25 $M_\odot$ to their reported He core mass values and find agreement of $\approx |0.6| - |3.7|$ %. Additionally, we compare the median values of C_{shell} to their quantity, M_{CO}^{01} which denotes

the mass coordinate where the main fuel for CO burning (^{4}He) drops below 10^{-2}. Our mass loss models with M_{ZAMS}=15, 20, and 25 $M_\odot$ agree to $\approx |0.3| - |8.8|$ % of their values.

The effect of nuclear and stellar input physics on pre-SN nucleosynthesis was considered by Rauscher et al. (2002). Their set of models were evolved using the 1D implicit hydrodynamics code, KEPLER (Weaver et al. 1978; Woosley & Weaver 1988; Heger et al. 2000), using a small nuclear network to generate the energy (similar to our approx22.net) with a larger adaptive network for the nucleosynthesis following $\approx$ 700–2200 nuclei from the MS to explosion. Overall, our median final Fe core mass at core-collapse agrees to within $\approx |1.8| - |7.0|$ % of their values. The largest difference is found when comparing the $M_{ZAMS} = 20\,M_\odot$ model. This, however, is not surprising and is stated in their investigation as possibly being a consequence of the merging of the O-, Ne-, and C-shells $\approx$ 1 day prior to collapse. We find considerable variation in the behavior of the O-, Ne-, and C-shells with the choice of whether they merge dependent on the resolution and network chosen. For instance our $25\,M_\odot$ and $30\,M_\odot$ models, the C-shell appears to 'merge' or dissolve prior to collapse. There is a large difference in the input physics of their models worthy of mention: the mass loss efficiency, convection parameterization, convective overshoot and other mixing terms. On average, their $20\,M_\odot$ and $25\,M_\odot$ models lose $\approx$ 2–5 $M_\odot$ more than our models.

Limongi et al. (2000) studied $13, 15, 20, 25\,M_\odot$, solar metallicity models with the FRANEC code (Chieffi et al. 1998) up to iron core collapse. Comparisons with their final state models they find $Y_{e,c} = 0.432, 0.435, 0.436$ for their $M_{ZAMS} = 15, 20, 25\,M_\odot$ models, the $15\,M_\odot$ models match our results while their 20 and $25\,M_\odot$ models have slightly lower $Y_{e,c}$ values, though within our upper and lower bounds on $Y_{e,c}$. They do not appear to have the ICZ we see in our models as they suppress overshoot and use the Schwarzschild criterion. They also artificially suppress the formation of CBP during core helium burning. Comparing the locations of the shell masses, our models in general predict shell locations to be $\approx 0.1\,M_\odot$ greater than those of Limongi et al. (2000). This may be due to differences in the choice of mixing parameters as well as the differences in behavior of the ICZ and SCZ between our models.

Sukhbold & Woosley (2014) studied the compactness of pre-SN cores in stars between $M_{ZAMS} = 15$–$65\,M_\odot$ with KEPLER. Comparing the compactness parameter, with their S-series models (non-rotating, solar metallicity, with mass loss), we have good agreement for the 15, 20 and $25\,M_\odot$ models for the compactness parameter measured when $v = 1000$ km s^{-1}. However for the $30\,M_\odot$ models, our value of $\xi_{M=2.5} \approx 0.6$ is much larger then their value of $\xi_{M=2.5} \approx 0.2$. Though this value is consistent with the lower edge of the values we find. KEPLER models do not reach $\xi_{M=2.5} \approx 0.6$ until $M_{ZAMS} \approx 35\,M_\odot$, though they point out that above $M_{ZAMS} = 30\,M_\odot$ uncertainties in mass loss can affect the results.

El Eid et al. (2004) studied $M_{ZAMS} = 15, 20, 25$ and $30\,M_\odot$ stars with mass loss up to the end of central oxygen burning using the code described in The et al. (2000). On average, comparing the core masses at the ignition of each fuel we find our models to be $0.5\,M_\odot$ heavier than those of El Eid et al. (2004). This can be explained as they use the Schwarzschild criterion everywhere and only study using Ledoux for convective boundaries in a $25\,M_\odot$ model. When they do use the Ledoux criteria (which we use everywhere) they find their core masses grow by $0.8\,M_\odot$ which places them within the values we find. Comparing the timescale to burn each fuel for the $15\,M_\odot$ and the $25\,M_\odot$ models, we find our values to be commensurate with their values, except for the length of carbon burning. For the $25\,M_\odot$ models without mass loss we find $\tau_c \approx 23$ yr, while they find $\tau_c \approx 1860$ yr. Differences may be due to the definition used. Comparing with their Figure 9, for the time over which carbon has vigorously ignited, they have carbon burning ≈ 100 yr however their burning is convective at the center, while we find carbon burning in the $25\,M_\odot$ to be radiative, likely due to the smaller core mass from using the Schwarzschild criteria.

One should bear in mind the limitations of our studies: our neglect of rotation and magnetic fields; ambiguous fidelity to the underlying 3D physics in the MESA 1D models: the treatment of convective (Trampedach et al. 2014), semiconvective (Moore & Garaud 2016), and overshoot (Kitiashvili et al. 2016) mixing; the parameterization of mass loss (e.g., Šurlan et al. 2012; Madura et al. 2013); potentially underestimated contributions from iron in the opacity (Blancard et al. 2012; Krief et al. 2016b,a; Turck-Chièze et al. 2016; Colgan et al. 2016); and unaccounted for uncertainties in the nuclear reaction rates (e.g., Sallaska et al. 2013; Fields et al. 2016).

This project was supported by NASA under the Theoretical and Computational Astrophysics Networks (TCAN) grant NNX14AB53G, by NSF under the Software Infrastructure for Sustained Innovation (SI^2) grant 1339600 and grant PHY 08-022648 for the Physics Frontier Center "Joint Institute for Nuclear Astrophysics - Center for the Evolution of the Elements" (JINA-CEE). L.D acknowledges financial support from "Agence Nationale de la Recherche" grant ANR-2011-Blanc-SIMI-5-007-01. C.E.F. acknowledges partial support from

Michigan State University under the College of Natural Sciences Early Start Fellowship Program. F.X.T. acknowledges sabbatical support from the Simons Foundation.

Software: `MESA` (Paxton et al. 2011, 2013, 2015), `Python` python.org, `matplotlib` (Hunter 2007), `NumPy` (van der Walt et al. 2011)

Facilities: Arizona State University Research Computing `Saguaro` and `Ocotillo` Systems.

REFERENCES

Aerts, C., Christensen-Dalsgaard, J., & Kurtz, D. W. 2010, Asteroseismology (Springer Science+Business Media B.V.)
Aerts, C., & Rogers, T. M. 2015, ApJ, 806, L33
Alastuey, A., & Jancovici, B. 1978, ApJ, 226, 1034
Arcones, A., Martínez-Pinedo, G., Roberts, L. F., & Woosley, S. E. 2010, A&A, 522, A25
Arnett, W. D. 1972a, ApJ, 176, 699
—. 1972b, ApJ, 173, 393
—. 1974, ApJ, 193, 169
—. 1996, Supernovae and Nucleosynthesis: An Investigation of the History of Matter, from the Big Bang to the Present (Princeton University Press)
Arnett, W. D., & Meakin, C. 2011, ApJ, 733, 78
Arnett, W. D., Meakin, C., Viallet, M., et al. 2015, ApJ, 809, 30
Arnett, W. D., & Thielemann, F.-K. 1985, ApJ, 295, 589
Arnett, W. D., & Truran, J. W. 1969, ApJ, 157, 339
Asida, S. M., & Arnett, D. 2000, ApJ, 545, 435
Asplund, M., Grevesse, N., Sauval, A. J., & Scott, P. 2009, ARA&A, 47, 481
Balasi, K. G., Langanke, K., & Martínez-Pinedo, G. 2015, Progress in Particle and Nuclear Physics, 85, 33
Baron, E., & Cooperstein, J. 1990, ApJ, 353, 597
Bazán, G., & Arnett, D. 1998, ApJ, 496, 316
Bennett, M. E., Hirschi, R., Pignatari, M., et al. 2012, MNRAS, 420, 3047
Blancard, C., Cossé, P., & Faussurier, G. 2012, ApJ, 745, 10
Bodansky, D., Clayton, D. D., & Fowler, W. A. 1968, ApJS, 16, 299
Boggs, S. E., Harrison, F. A., Miyasaka, H., et al. 2015, Science, 348, 670
Böhm-Vitense, E. 1958, ZA, 46, 108
Boothroyd, A. I., Sackmann, I.-J., & Ahern, S. C. 1993, ApJ, 416, 762
Brown, J. M., Garaud, P., & Stellmach, S. 2013, ApJ, 768, 34
Bruenn, S. W., Lentz, E. J., Hix, W. R., et al. 2016, ApJ, 818, 123
Busso, M., & Gallino, R. 1985, A&A, 151, 205
Caputo, F., Chieffi, A., Tornambe, A., Castellani, V., & Pulone, L. 1989, ApJ, 340, 241
Castellani, V., Chieffi, A., Tornambe, A., & Pulone, L. 1985, ApJ, 296, 204
Chatzopoulos, E., Couch, S. M., Arnett, W. D., & Timmes, F. X. 2016, ApJ, 822, 61
Chatzopoulos, E., & Wheeler, J. C. 2012, ApJ, 748, 42
Chen, M. C., Herwig, F., Denissenkov, P. A., & Paxton, B. 2014, MNRAS, 440, 1274
Chieffi, A., & Limongi, M. 2013, ApJ, 764, 21
Chieffi, A., Limongi, M., & Straniero, O. 1998, ApJ, 502, 737
Choi, J., Dotter, A., Conroy, C., et al. 2016, ApJ, 823, 102
Clifford, F. E., & Tayler, R. J. 1965, MmRAS, 69, 21
Coc, A., Goriely, S., Xu, Y., Saimpert, M., & Vangioni, E. 2012, ApJ, 744, 158
Colgan, J., Kilcrease, D. P., Magee, N. H., et al. 2016, ApJ, 817, 116
Constantino, T., Campbell, S. W., Lattanzio, J. C., & van Duijneveldt, A. 2016, MNRAS, 456, 3866
Couch, S. M., Chatzopoulos, E., Arnett, W. D., & Timmes, F. X. 2015, ApJL, 808, L21
Couch, S. M., & O'Connor, E. P. 2014, ApJ, 785, 123
Cox, J. P., & Giuli, R. T. 1968, Principles of Stellar Structure (New York: Gordon & Breach)
Creevey, O. L., Thévenin, F., Berio, P., et al. 2015, A&A, 575, A26
Cyburt, R. H., Fields, B. D., Olive, K. A., & Yeh, T.-H. 2016, Reviews of Modern Physics, 88, 015004
Cyburt, R. H., Amthor, A. M., Ferguson, R., et al. 2010, ApJS, 189, 240
Denissenkov, P. A., Herwig, F., Truran, J. W., & Paxton, B. 2013, ApJ, 772, 37
Dessart, L., Hillier, D. J., Waldman, R., & Livne, E. 2013, MNRAS, 433, 1745
Dessart, L., Livne, E., & Waldman, R. 2010, MNRAS, 408, 827
Doherty, C. L., Gil-Pons, P., Lau, H. H. B., Lattanzio, J. C., & Siess, L. 2014, MNRAS, 437, 195
Dolence, J. C., Burrows, A., Murphy, J. W., & Nordhaus, J. 2013, ApJ, 765, 110
El Eid, M. F., Meyer, B. S., & The, L.-S. 2004, ApJ, 611, 452
Eldridge, J. J., & Tout, C. A. 2004, MNRAS, 353, 87
Endal, A. S. 1975, ApJ, 195, 187
Farmer, R., Fields, C. E., & Timmes, F. X. 2015, ApJ, 807, 184
Fields, B. D., Olive, K. A., Vangioni-Flam, E., & Cassé, M. 2000, ApJ, 540, 930
Fields, C. E., Farmer, R., Petermann, I., Iliadis, C., & Timmes, F. X. 2016, ApJ, 823, 46
Fuller, G. M., Fowler, W. A., & Newman, M. J. 1985, ApJ, 293, 1
Fuller, J., Cantiello, M., Stello, D., Garcia, R. A., & Bildsten, L. 2015, Science, 350, 423
Garaud, P., Medrano, M., Brown, J. M., Mankovich, C., & Moore, K. 2015, ApJ, 808, 89
Gibson, B. K., Fenner, Y., Renda, A., Kawata, D., & Lee, H. 2003, PASA, 20, 401
Glebbeek, E., Gaburov, E., de Mink, S. E., Pols, O. R., & Portegies Zwart, S. F. 2009, A&A, 497, 255
Grevesse, N., & Sauval, A. J. 1998, SSRv, 85, 161
Hansen, C. J., Kawaler, S. D., & Trimble, V. 2004, Stellar interiors : physical principles, structure, and evolution (New York: Springer-Verlag)
Hartmann, D., Woosley, S. E., & El Eid, M. F. 1985, ApJ, 297, 837
Heger, A., Langer, N., & Woosley, S. E. 2000, ApJ, 528, 368
Heger, A., & Woosley, S. E. 2010, ApJ, 724, 341
Heger, A., Woosley, S. E., Martínez-Pinedo, G., & Langanke, K. 2001, ApJ, 560, 307
Herwig, F., Bloecker, T., Schoenberner, D., & El Eid, M. 1997, A&A, 324, L81
Hirschi, R., Meynet, G., & Maeder, A. 2004, A&A, 425, 649
Hix, W. R., & Thielemann, F.-K. 1996, ApJ, 460, 869
—. 1999, ApJ, 511, 862
Hoppe, P., Leitner, J., Gröner, E., et al. 2010, ApJ, 719, 1370
Humphreys, R. M., & Davidson, K. 1994, PASP, 106, 1025
Hunter, J. D. 2007, Computing In Science & Engineering, 9, 90

Iben, Jr., I. 2013a, Stellar Evolution Physics, Volume 1: Physical Processes in Stellar Interiors (Cambridge, UK: Cambridge University Press)
—. 2013b, Stellar Evolution Physics, Volume 2: Advanced Evolution of Single Stars (Cambridge, UK: Cambridge University Press)
Iben, Jr., I., & Truran, J. W. 1978, ApJ, 220, 980
Iliadis, C. 2007, Nuclear Physics of Stars (Wiley-VCH Verlag)
Iliadis, C., Champagne, A., Chieffi, A., & Limongi, M. 2011, ApJS, 193, 16
Itoh, N., Hayashi, H., Nishikawa, A., & Kohyama, Y. 1996, ApJS, 102, 411
Itoh, N., Totsuji, H., Ichimaru, S., & Dewitt, H. E. 1979, ApJ, 234, 1079
Janka, H.-T. 2012, Annual Review of Nuclear and Particle Science, 62, 407
Jerkstrand, A., Timmes, F. X., Magkotsios, G., et al. 2015, ApJ, 807, 110
Jiang, Y.-F., Cantiello, M., Bildsten, L., Quataert, E., & Blaes, O. 2015, ApJ, 813, 74
Jones, S., Andrassy, R., Sandalski, S., et al. 2016, ArXiv e-prints, arXiv:1605.03766
Jones, S., Hirschi, R., Nomoto, K., et al. 2013, ApJ, 772, 150
Jordan, IV, G. C., & Meyer, B. S. 2004, ApJL, 617, L131
Justham, S., Podsiadlowski, P., & Vink, J. S. 2014, ApJ, 796, 121
Karakas, A. I., & Lugaro, M. 2016, ApJ, 825, 26
Kashi, A., Davidson, K., & Humphreys, R. M. 2016, ApJ, 817, 66
Kippenhahn, R., Ruschenplatt, G., & Thomas, H.-C. 1980, A&A, 91, 175
Kippenhahn, R., Weigert, A., & Weiss, A. 2012, Stellar Structure and Evolution (Springer-Verlag: Berlin)
Kitiashvili, I. N., Kosovichev, A. G., Mansour, N. N., & Wray, A. A. 2016, ApJL, 821, L17
Kossert, K., & Günther, E. 2004, Applied Radiation and Isotopes, 60, 459 , proceedings of the 14th International Conference on Radionuclide Metrology and its Applications, {ICRM} 2003
Krief, M., Feigel, A., & Gazit, D. 2016a, ApJ, 824, 98
—. 2016b, ApJ, 821, 45
Lamb, S. A., Iben, Jr., I., & Howard, W. M. 1976, ApJ, 207, 209
Langanke, K., & Martínez-Pinedo, G. 2000, Nuclear Physics A, 673, 481
Langer, N. 1991, A&A, 252, 669
Langer, N., El Eid, M. F., & Fricke, K. J. 1985, A&A, 145, 179
Langer, N., Fricke, K. J., & Sugimoto, D. 1983, A&A, 126, 207
Lewis, K. M., Lugaro, M., Gibson, B. K., & Pilkington, K. 2013, ApJL, 768, L19
Limongi, M., & Chieffi, A. 2003, ApJ, 592, 404
Limongi, M., Straniero, O., & Chieffi, A. 2000, ApJS, 129, 625
Lugaro, M., Zinner, E., Gallino, R., & Amari, S. 1999, ApJ, 527, 369
Madura, T. I., Gull, T. R., Okazaki, A. T., et al. 2013, MNRAS, 436, 3820
Maeder, A., & Meynet, G. 2001, A&A, 373, 555
—. 2012, Reviews of Modern Physics, 84, 25
Magkotsios, G., Timmes, F. X., Hungerford, A. L., et al. 2010, ApJS, 191, 66
Malonda, A. G., & Carles, A. G. 2002, Applied Radiation and Isotopes, 56, 153 , proceedings of the Conference on Radionuclide Metrology and its A pplications, ICRM'01
Marchant, P., Langer, N., Podsiadlowski, P., Tauris, T. M., & Moriya, T. J. 2016, A&A, 588, A50
Meakin, C. A., & Arnett, D. 2007a, ApJ, 665, 690
—. 2007b, ApJ, 667, 448
Meyer, B. S., Krishnan, T. D., & Clayton, D. D. 1998, ApJ, 498, 808
Miglio, A., & Montalbán, J. 2005, A&A, 441, 615
Moll, R., Garaud, P., & Stellmach, S. 2016, ApJ, 823, 33
Moore, K., & Garaud, P. 2016, ApJ, 817, 54
Mowlavi, N., & Forestini, M. 1994, A&A, 282, 843
Müller, B., Viallet, M., Heger, A., & Janka, H.-T. 2016, ArXiv e-prints, arXiv:1605.01393
Nadyozhin, D. K., & Yudin, A. V. 2004, Astronomy Letters, 30, 634
Nieuwenhuijzen, H., & de Jager, C. 1990, A&A, 231, 134
Noels, A., Grevesse, N., Magain, P., et al. 1991, A&A, 247, 91
Nomoto, K., & Hashimoto, M. 1988, PhR, 163, 13
Nomoto, K., Kobayashi, C., & Tominaga, N. 2013, ARA&A, 51, 457
Nugis, T., & Lamers, H. J. G. L. M. 2000, A&A, 360, 227
O'Connor, E., & Ott, C. D. 2011, ApJ, 730, 70
Oda, T., Hino, M., Muto, K., Takahara, M., & Sato, K. 1994, Atomic Data and Nuclear Data Tables, 56, 231
Ofek, E. O., Sullivan, M., Shaviv, N. J., et al. 2014, ApJ, 789, 104
Olive, K. A., & Schramm, D. N. 1992, Nature, 360, 439
Ott, C. D., Abdikamalov, E., Mösta, P., et al. 2013, ApJ, 768, 115
Özel, F., Psaltis, D., Ransom, S., Demorest, P., & Alford, M. 2010, ApJ, 724, L199
Papadopoulos, A., D'Andrea, C. B., Sullivan, M., et al. 2015, MNRAS, 449, 1215
Paxton, B., Bildsten, L., Dotter, A., et al. 2011, ApJS, 192, 3
Paxton, B., Cantiello, M., Arras, P., et al. 2013, ApJS, 208, 4
Paxton, B., Marchant, P., Schwab, J., et al. 2015, ApJS, 220, 15
Pejcha, O., & Thompson, T. A. 2015, ApJ, 801, 90
Peng, T.-C., Humphreys, E. M. L., Testi, L., et al. 2013, A&A, 559, L8
Perego, A., Hempel, M., Fröhlich, C., et al. 2015, ApJ, 806, 275
Petermann, I., Langer, N., Castro, N., & Fossati, L. 2015, A&A, 584, A54
Prantzos, N. 2012, A&A, 542, A67
Rakavy, G., Shaviv, G., & Zinamon, Z. 1967, ApJ, 150, 131
Ramaty, R., Scully, S. T., Lingenfelter, R. E., & Kozlovsky, B. 2000, ApJ, 534, 747
Rauscher, T., Heger, A., Hoffman, R. D., & Woosley, S. E. 2002, ApJ, 576, 323
Rauscher, T., & Thielemann, F.-K. 2000, Atomic Data and Nuclear Data Tables, 75, 1
Reeves, H., Fowler, W. A., & Hoyle, F. 1970, Nature, 226, 727
Renzini, A., & Voli, M. 1981, A&A, 94, 175
Rogers, T. M. 2015, ApJ, 815, L30
Rogers, T. M., Lin, D. N. C., McElwaine, J. N., & Lau, H. H. B. 2013, ApJ, 772, 21
Sacco, G. G., Jeffries, R. D., Randich, S., et al. 2015, A&A, 574, L7
Sallaska, A. L., Iliadis, C., Champange, A. E., et al. 2013, ApJS, 207, 18
Seitenzahl, I. R., Timmes, F. X., Marin-Laflèche, A., et al. 2008, ApJ, 685, L129
Smith, N., Andrews, J. E., Van Dyk, S. D., et al. 2016, MNRAS, 458, 950
Spruit, H. C. 2013, A&A, 552, A76
Straniero, O., Domínguez, I., Imbriani, G., & Piersanti, L. 2003, ApJ, 583, 878
Strotjohann, N. L., Ofek, E. O., Gal-Yam, A., et al. 2015, ApJ, 811, 117
Sukhbold, T., Ertl, T., Woosley, S. E., Brown, J. M., & Janka, H.-T. 2016, ApJ, 821, 38
Sukhbold, T., & Woosley, S. E. 2014, ApJ, 783, 10
The, L.-S., Clayton, D. D., Jin, L., & Meyer, B. S. 1998, ApJ, 504, 500
The, L.-S., El Eid, M. F., & Meyer, B. S. 2000, ApJ, 533, 998
Thielemann, F. K., & Arnett, W. D. 1985, ApJ, 295, 604
Timmes, F. X., & Clayton, D. D. 1996, ApJ, 472, 723

Timmes, F. X., Woosley, S. E., & Weaver, T. A. 1995, ApJS, 98, 617
—. 1996, ApJ, 457, 834
Trampedach, R., Stein, R. F., Christensen-Dalsgaard, J., Nordlund, Å., & Asplund, M. 2014, MNRAS, 445, 4366
Traxler, A., Garaud, P., & Stellmach, S. 2011, ApJ, 728, L29
Turck-Chièze, S., Le Pennec, M., Ducret, J. E., et al. 2016, ApJ, 823, 78
Ulrich, R. K. 1972, ApJ, 172, 165
Šurlan, B., Hamann, W.-R., Kubát, J., Oskinova, L. M., & Feldmeier, A. 2012, A&A, 541, A37
van der Walt, S., Colbert, S. C., & Varoquaux, G. 2011, Computing in Science Engineering, 13, 22
Van Dyk, S. D., Peng, C. Y., King, J. Y., et al. 2000, PASP, 112, 1532
Viallet, M., Meakin, C., Arnett, D., & Mocák, M. 2013, ApJ, 769, 1
Vink, J. S., de Koter, A., & Lamers, H. J. G. L. M. 2001, A&A, 369, 574
Vitense, E. 1953, ZA, 32, 135
Vreeswijk, P. M., Savaglio, S., Gal-Yam, A., et al. 2014, ApJ, 797, 24
Wasserburg, G. J., Trippella, O., & Busso, M. 2015, ApJ, 805, 7
Weaver, T. A., Zimmerman, G. B., & Woosley, S. E. 1978, ApJ, 225, 1021
Wellstein, S., & Langer, N. 1999, A&A, 350, 148
West, C., Heger, A., & Austin, S. M. 2013, ApJ, 769, 2
Wheeler, J. C., Kagan, D., & Chatzopoulos, E. 2015, ApJ, 799, 85
Wiescher, M., Käppeler, F., & Langanke, K. 2012, ARA&A, 50, 165
Woosley, S. E., Arnett, W. D., & Clayton, D. D. 1972, ApJ, 175, 731
—. 1973, ApJS, 26, 231
Woosley, S. E., Hartmann, D. H., Hoffman, R. D., & Haxton, W. C. 1990, ApJ, 356, 272
Woosley, S. E., Heger, A., & Weaver, T. A. 2002, Rev. Mod. Phys., 74, 1015
Woosley, S. E., & Hoffman, R. D. 1992, ApJ, 395, 202
Woosley, S. E., & Weaver, T. A. 1988, PhR, 163, 79
—. 1995, ApJS, 101, 181
Yoon, S.-C., Langer, N., & Norman, C. 2006, A&A, 460, 199
Yuan, F., Lidman, C., Davis, T. M., et al. 2015, MNRAS, 452, 3047
Zaussinger, F., & Spruit, H. C. 2013, A&A, 554, A119
Zavagno, A., Anderson, L. D., Russeil, D., et al. 2010, A&A, 518, L101